



1

2

## Size-Resolved Dust Direct Radiative Effect Efficiency

3

### Derived from Satellite Observations

4

Qianqian Song<sup>1,2,\*</sup>, Zhibo Zhang<sup>1,2</sup>, Hongbin Yu<sup>3</sup>, Jasper F. Kok<sup>4</sup>, Claudia Di Biagio<sup>5</sup>,

5

Samuel Albani<sup>6</sup>, Jianyu Zheng<sup>1,2</sup>, Jiachen Ding<sup>7</sup>

6

7

1. Physics Department, UMBC, Baltimore, Maryland, USA

8

2. Goddard Earth Sciences Technology and Research II, UMBC, Baltimore, Maryland, USA

9

3. Climate and Radiation Laboratory, NASA Goddard Space Flight Center, Greenbelt,  
Maryland, USA

10

4. Department of Atmospheric and Oceanic Sciences, University of California, Los  
Angeles, CA 90095, USA

11

12

5. Université de Paris Cité and Université Paris Est Creteil, CNRS, LISA, F-75013 Paris,  
France

13

14

6. Department of Environmental and Earth Sciences, University of Milano–Bicocca, Milan,  
Italy

15

16

7. Department of Atmospheric Sciences, Texas A&M University, College Station, Texas,  
USA

17

18

19

20

\*Correspondence to: Qianqian Song

21

Email: cd11735@umbc.edu

22

23



24 **Abstract**

25           The role of mineral dust aerosol in global radiative energy budget is often quantified by  
26 the dust direct radiative effect (DRE). The dust DRE strongly depends on dust aerosol optical  
27 depth (DAOD), therefore, DRE efficiency ( $DREE=DRE/DAOD$ ) is widely compared across  
28 different studies to eliminate difference due to the various dust load. Nevertheless, DREE is still  
29 influenced by the uncertainties associated with dust particle size distribution (PSD) and optical  
30 properties. In this study, we derive a global clear-sky *size-resolved* DREE dataset in both  
31 shortwave (SW) and longwave (LW) at top of the atmosphere (TOA) and surface based on satellite  
32 observations (i.e., satellite-retrieved dust extinction spatial and vertical distributions). In the DREE  
33 dataset, dust geometric diameter from  $0.1\mu\text{m}$  to  $100\mu\text{m}$  is divided into 10 bins and the  
34 corresponding monthly mean DREE (with respect to DAOD at 532nm) for each size bin is derived  
35 by using the Rapid Radiative Transfer Model (RRTM). Three sets of state-of-the-art dust refractive  
36 indices (RI) and two sets of dust shape models (sphere vs. spheroid) are adopted to investigate the  
37 sensitivity of dust DREE to dust absorption and shape. As a result, the size-resolved dust DREE  
38 dataset contains globally distributed monthly mean dust DREE at TOA and surface for each of 10  
39 size bins with  $5^\circ$  (longitude)  $\times$   $2^\circ$  (latitude) resolution as well as for each dust RI and shape  
40 combination. The size-resolved dust DREE dataset can be used to readily calculate global dust  
41 DRE for any DAOD and dust PSD, including the uncertainty in the DRE induced by dust  
42 microphysical properties (e.g., dust PSD, RI and shape). By calculating dust DRE based on DAOD  
43 climatology retrieved from different satellite sensors and based on different dust PSD, we find that  
44 uncertainty in the spatial pattern of DAOD induces more than 10% of the uncertainty in SW dust  
45 DRE at TOA. The observation-based dust PSD induces around 15%~20% uncertainty in dust DRE  
46 at TOA and in the atmosphere. The sensitivity assessments of dust DRE to dust RI and shape



47 further suggest that dust non-sphericity induces a negligible effect on dust DRE estimations, while  
48 dust RI turns out to be the most important factor in determining dust DRE, particularly in SW.  
49



50

## 51 **1 Introduction**

52 Mineral dust is an important component of the atmospheric aerosol (Textor et al., 2006;  
53 Choobari et al., 2014). They can influence the radiative energy budget of the Earth-Atmosphere  
54 system directly through their interaction with both solar and thermal infrared radiation, which is  
55 known as the direct radiative effect (DRE) of dust. The DRE of dust consists of two components.  
56 In the solar shortwave (SW) spectral region, dust aerosols reflect a fraction of solar radiation back  
57 to the space which generally leads to a negative cooling effect at both top of the atmosphere (TOA)  
58 and surface (Tegen et al., 1996; Myhre et al., 2003). In the longwave (LW) thermal infrared region,  
59 dust aerosols trap the thermal radiation emitted from Earth's surface by absorption, which  
60 generally leads to a positive warming radiative effect at TOA and surface (Sokolik et al., 1998).  
61 In addition to DRE, dust can also influence the radiation and the hydrological cycles indirectly  
62 through serving as cloud condensation nuclei and ice nuclei and affecting cloud microphysical  
63 properties and cloud lifetime, known as indirect effects of dust (Twomey, 1977; Albrecht, 1989).

64 The dust DRE depends on many factors including primarily the atmospheric dust content,  
65 represented by its optical depth (DAOD), vertical distribution (especially important for LW DRE),  
66 and particles' physico-chemical properties that are the particle size distribution (PSD), complex  
67 refractive index (RI), and shape. Besides dust PSD, RI and shape, the dust DRE also depends on  
68 the atmospheric composition and structure, notably the atmospheric vertical profile of clouds,  
69 water vapor, and temperature, as well as surface properties (Yu et al., 2006). All of these properties  
70 vary in space and time and need to be characterized at the best possible spatio-temporal resolution  
71 in order to get realistic dust DRE estimates.



72           Among all these factors, DAOD is of first order importance in determining dust DRE since  
73 dust DRE is approximately linear with DAOD (Satheesh and Ramanathan, 2000). Many previous  
74 studies related to dust DRE are based on DAOD distributions from model simulations. For  
75 example, Kok et al. (2017) used four global model simulations to estimate global mean dust DRE  
76 efficiency (DREE is defined as DRE/DAOD) and further derive global mean dust DRE. Di Biagio  
77 et al. (2020) derived dust DRE based on model-simulated DAOD distributions with global annual  
78 mean DAOD constrained by observations. The main advantage of these studies is the availability  
79 of continuous and detailed DAOD spatial and temporal variation from model simulations. On the  
80 other hand, model-simulated DAOD could be subject to large uncertainties and biases in  
81 reproducing DAOD due to parameterizations of various physical processes, therefore need  
82 observational constraints for evaluation and improvement.

83           Satellite observations are important sources of data for evaluating model simulations,  
84 because of their routine sampling on a global scale and over decadal time periods. Previous studies  
85 have developed sensor-specific methods to distinguish dust aerosol from total aerosol based on the  
86 size and shape characteristics of dust particles. Some are based on passive satellite observations  
87 such as Moderate Resolution Imaging Spectroradiometer (MODIS, Remer et al. (2005)) and others  
88 are based on active observations such as Cloud-Aerosol Lidar with Orthogonal Polarization  
89 (CALIOP, Winker et al. (2009)). The wide spectral coverage of MODIS measurements allows the  
90 retrieval of aerosol particle size information, such as effective radius, fine-mode fraction, aerosol  
91 Angstrom exponent, as well as spectral gradient of absorption (Remer et al., 2005; Hsu et al., 2013).  
92 Based on the fact that dust aerosols are generally larger in size than other aerosols and have a  
93 decreasing absorption from ultraviolet (UV) to the near infrared, the combinations of these  
94 retrievals provide the basis for dust separation and dust aerosol optical depth (DAOD) retrievals



95 from MODIS (Kaufman et al., 2005; Ginoux et al., 2012; Voss and Evan, 2020; Yu et al., 2009,  
96 2019). In addition, some recent studies have also characterized dust distribution through  
97 integrating MODIS measurements with other data sources and model simulations, for example,  
98 using the DAOD-to-AOD ratio from MERRA-2 (Modern-Era Retrospective analysis for Research  
99 and Applications, version 2 ), Gkikas et al. (2021) converted the MODIS AOD retrievals to DAOD.  
100 However, passive sensors do not provide the vertical structure of aerosol that is critical for studying  
101 aerosol–cloud interactions, LW radiative effects and aerosol influences on the thermal structure of  
102 the atmosphere (e.g., Meloni et al., 2005, 2015). By contrast, the active sensor CALIOP can  
103 provide the vertical profiles of aerosol extinction and particle properties such as depolarization  
104 ratio and color ratio, which have been used for improving DAOD retrievals in thermal infrared  
105 (TIR) (Zheng et al., 2022) and evaluating global dust simulations (Yu et al., 2010; Wu et al., 2020).  
106 The CALIOP dust identification is mainly based on dust aerosols being non-spherical in shape and  
107 their linear depolarization ratio being much larger than spherical aerosols (Sakai et al., 2010).

108 Using CALIOP retrievals, Song et al. (2021) derived a three-dimensional (3D) decadal  
109 (2007-2019) global scale dust extinction profile climatology, which provides an observational  
110 constraint on both the spatial DAOD pattern and the vertical dust distribution for studying dust  
111 DRE and evaluating models. In their study, Song et al. (2021) also compared dust retrievals, in  
112 particular DAOD, based on different methods and showed that DAOD often differ significantly  
113 between the different products. For example, they showed that DAOD derived from CALIOP  
114 observations is generally smaller and more concentrated over ‘dust belt’ regions - extending from  
115 the west coast of north Africa to the Middle East, central Asia, and China - than that derived from  
116 MODIS observations. These differences in DAOD in turn lead to different dust DRE estimations,  
117 making it difficult to compare different studies to reach meaningful conclusions. Even an



118 agreement of DRE could be a result of the compensation between differences in DAOD and other  
119 aforementioned factors, such as dust microphysical properties. Therefore, DRE provides only a  
120 weak constraint on model. Instead, a normalized quantity, DRE efficiency (DREE) as the ratio of  
121 DRE to DAOD, has been widely used in inter-comparison studies and model evaluations (Di  
122 Biagio et al. 2020). Because of the elimination of DAOD, the DREE provides a stronger constraint  
123 on dust microphysical properties and their impacts on the dust DRE from different dust source  
124 regions (García et al., 2008).

125 In addition to DAOD, dust size is also an important factor in determining dust DRE  
126 (Mahowald et al., 2014). Smaller particles are more effective at scattering SW radiation and super-  
127 micron particles are more effective at absorbing both SW and LW radiation (Tegen and Lacis,  
128 1996). Therefore, when other parameters are equal, fine dust would generally have a more negative  
129 SW DRE and a less positive LW DRE than coarse dust. Unfortunately, despite its importance, the  
130 simulation of dust PSD in the models and satellite retrievals of dust size remain challenging tasks  
131 (Ryder et al., 2019). As a result, there is a large uncertainty in our understanding of dust PSD. For  
132 example, several recent studies suggested that model simulations tend to underestimate dust size,  
133 especially the very coarse dust with diameter in excess of 5  $\mu\text{m}$  (Adebisi and Kok, 2020).  
134 Moreover, dust RI and shape can be important for DRE estimation as well because besides dust  
135 PSD they are the other two factors that determine dust spectral optical properties. As such, it is  
136 important to investigate the sensitivity of dust DRE to dust PSD, RI and shape. Previous studies  
137 suggest that large dust PSD and RI uncertainty leads to a large uncertainty in dust DRE and thereby  
138 DREE estimations. For example, Song et al., (2018) shows that the SW DREE of a dust model  
139 with a large size and less absorptive RI is very similar to that of a dust model with a smaller size  
140 and more absorptive RI, both in the range of satellite derived values in the NE Atlantic region. Not



141 surprisingly, even DREE cannot provide sufficient constraints due to this possible compensation  
142 of effects in the dust PSD and RI.

143 The main objective of this study is to derive a global clear-sky size-resolved dust DREE  
144 dataset based on satellite observations and demonstrate its usefulness in constraining, comparing,  
145 and understanding the dust DRE estimations. As explained below, the size-resolved DREE  
146 decomposes the DREE of dust into several size bins and therefore provide a way to take into  
147 account the effects of dust PSD explicitly. The sensitivity of dust DRE to dust RI and shape are  
148 also assessed in this study. Due to the inhomogeneous spatio-temporal distribution of those  
149 aforementioned factors, it is thus important to consider the spatio-temporal variation of dust DREE.  
150 Therefore, we organize the DREE dataset at  $5^\circ$  (longitude)  $\times$   $2^\circ$  (latitude) horizontal resolution  
151 and at monthly temporal resolution. To the best of our knowledge, this work presents the first such  
152 dataset based on retrieved dust properties (i.e., DAOD vertical and horizontal distributions) from  
153 satellite observations, although size-resolved DREE from model simulations have been used in  
154 previous studies. We will show that our size-resolved DREE can allow users to readily compute  
155 the DREE and DRE of dust based on any dust PSD (e.g., from model simulations, satellite  
156 retrievals or in-situ measurements). We will also carry out an inter-comparison of the global dust  
157 DRE estimations based on different dust PSD and compare the results with previous studies. With  
158 these functions, we expect that the size-resolved DREE will be a useful tool for both observational  
159 and modeling studies of dust DRE.

160 The rest of the paper is organized as follows. Section 2 provides a description of the data  
161 and models used in this study. Section 3 describes the methodology of deriving the size-resolved  
162 DREE dataset. In section 4, we describe a methodology of calculating the dust DRE with the size-  
163 resolved DREE dataset and its validation. In section 5, we compare the regional and global dust



164 DRE estimations based on different DAOD, dust PSD and compare the results with previous  
165 studies. Section 6 provides a summary of the study along with the main conclusions.

## 166 **2 Data and Models**

### 167 **2.1 Satellite-based DAOD climatology**

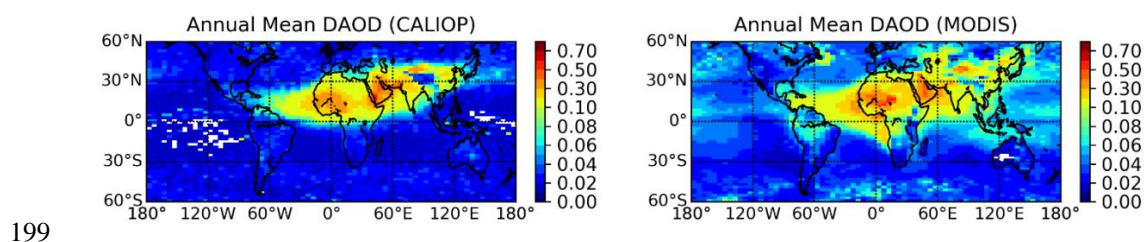
168 We use CALIOP-based DAOD climatology and dust vertical distribution derived in Song  
169 et al. (2021) to derive a size-resolved dust DREE. The reason for choosing CALIOP-based DAOD  
170 climatology is discussed in detail in section 3.2. The CALIOP-based dust climatology dataset  
171 contains monthly mean DAOD and dust vertical extinction profile on a  $5^\circ$  (longitude)  $\times$   $2^\circ$   
172 (latitude) spatial resolution grid for the period 2007-2019. The CALIOP-based DAOD and dust  
173 vertical distribution climatology from 2007 to 2010 are used to derive monthly mean size-resolved  
174 dust DREE dataset in this study. The selection of 4 years (2007-2010) for DREE calculations is  
175 based on several considerations. Firstly, the multi-year DREE calculations allow us to investigate  
176 the effect of interannual variations of atmospheric and surface properties to dust DRE. Secondly,  
177 this selection is consistent with Song et al. (2018), making it easier to compare our results with  
178 previous work. Thirdly, considering the computational efficiency, we do not extend the calculation  
179 to more years.

180 In addition to CALIOP-based DAOD climatology, we will use the MODIS-based DAOD  
181 climatology to investigate the sensitivity of dust DRE to DAOD spatial pattern in section 5.2. The  
182 MODIS-based DAOD climatology achieves global coverage on a  $5^\circ$  (longitude)  $\times$   $2^\circ$  (latitude)  
183 spatial resolution for the period 2003-2019 by combining the monthly mean Aqua MODIS over-  
184 ocean (Yu et al., 2020) and over-land (Pu and Ginoux, 2018) DAOD. In contrast to CALIOP-based  
185 DAOD climatology which is based on dust non-sphericity to separate dust aerosol from CALIOP  
186 total aerosol observations, MODIS-based DAOD retrieval is mainly based on dust large size to



187 partition DAOD from MODIS total aerosol observations. The two sensor-specific dust partition  
188 methods result in different DAOD magnitude and spatial pattern retrievals.

189 Figure 1 shows annual mean DAOD from 2007 to 2010 based on CALIOP and MODIS  
190 observations. CALIOP-based and MODIS-based DAOD climatology differ in terms of both  
191 magnitude and spatial pattern. MODIS-based DAOD is generally larger than CALIOP-based  
192 DAOD. For example, the global ( $60^{\circ}\text{S} - 60^{\circ}\text{N}$ ) 4-year mean MODIS-based DAOD is 0.047, while  
193 CALIOP-based DAOD is 0.032. High DAOD are seen from both CALIOP-based and MODIS-  
194 based DAOD over the ‘dust belt’ regions, where large-scale dust activities occur persistently  
195 throughout the year. However, the CALIOP-based DAOD is rather low in some other regions that  
196 are known to be dusty in certain seasons, such as southwestern United States, South America,  
197 Australia, and South Africa. In other words, the two satellite-based DAOD spatial pattern differs  
198 significantly with CALIOP-based DAOD more concentrated over ‘dust belt’ regions.



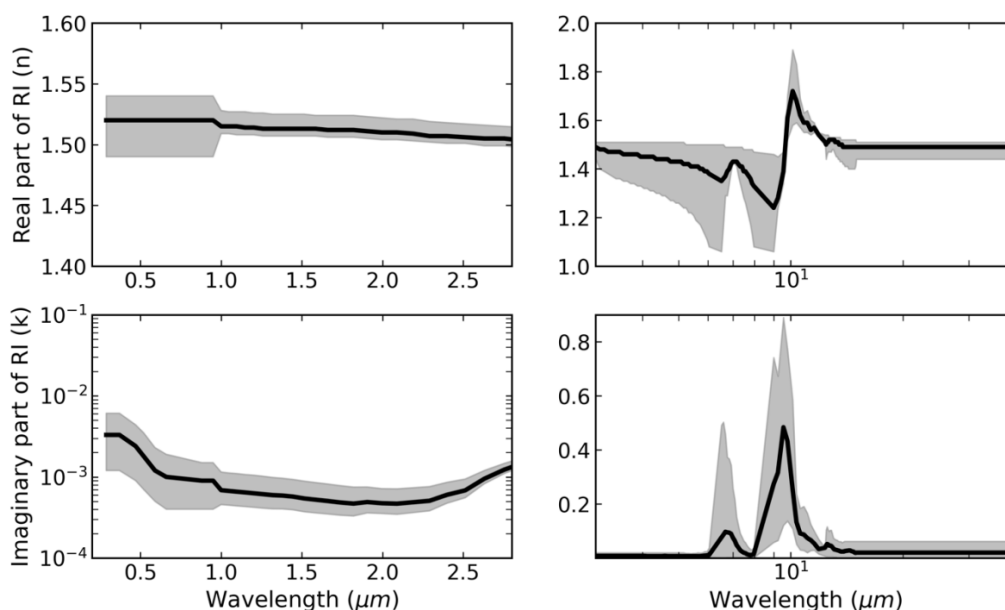
200 Figure 1. Global ( $60^{\circ}\text{S} - 60^{\circ}\text{N}$ ) spatial pattern of CALIOP-based and MODIS-based 4-year (2007-2010) mean  
201 DAOD (Song et al., 2021).

## 202 2.2 Dust physical and optical models

203 To study the sensitivity of dust DREE to dust RI and dust shape, we adopt three sets of  
204 dust RI (Figure 2) and two dust shapes (Figure 4 (a) in Song et al. 2018) and compute a total of 6  
205 sets of DREE based on their combinations. The three dust RI sets represent less absorptive, mean  
206 absorptive and more absorptive dust aerosols and the two dust shapes include spherical and  
207 spheroidal dust shapes. The mean, 10<sup>th</sup> and 90<sup>th</sup> percentile of calculated RI for 19 dust samples



208 over 8 regions in Di Biagio et al. (2019) are used to represent mean, less and more absorptive dust  
209 in SW. We combine RI of wavelengths from  $0.37\mu\text{m}$  to  $0.95\mu\text{m}$  measured in Di Biagio et al.  
210 (2019) and RI of other wavelengths up to  $3\mu\text{m}$  reported in Balkanski et al. (2007) to get full  
211 spectral coverage in SW. The mean, minimum and maximum RI of wavelengths beyond  $3\mu\text{m}$   
212 measured in Di Biagio et al. (2017) are used to represent mean, less and more absorptive dust in  
213 LW. Two dust shapes are used to investigate the effect of dust nonsphericity on dust DRE. One is  
214 spherical dust shape, the other one is spheroidal dust shape with dust aspect ratio distribution  
215 described by Figure 4 (a) in Song et al. (2018) which is originally from Dubovik et al. (2006).  
216 Each combination of dust RI and dust shape is considered as a dust model. As a result, the three  
217 dust RI and two dust shapes constitute six dust models in SW and LW, respectively, as shown in  
218 Table 1.



219

220 Figure 2. The SW and LW spectral refractive indices (RI) used in this study. The black curves represent the mean RI  
221 which indicates the mean absorptive dust. The grey shading represents the upper and lower limits indicating more  
222 absorptive and less absorptive dust, respectively. References for the used datasets are provided in Section 2.2.



223 Table 1. Dust models used in this study. Three dust RI are used in shortwave (SW) and longwave (LW) to represent  
224 less, mean, and more absorptive dust, respectively. Two dust shape models are used to represent spherical and  
225 spheroidal dust shape. The three dust RI sets and two dust shapes constitute 6 dust models in SW and LW respectively.

	SW RI (Balkanski et al. 2007; Di Biagio et al. 2019)			LW RI (Di Biagio et al. 2017)		
	10%	Mean	90%	Minimum	Mean	Maximum
Sphere	MinSWRI-Sphere	MeanSWRI-Sphere	MaxSWRI-Sphere	MinLWRI-Sphere	MeanLWRI-Sphere	MaxLWRI-Sphere
Spheroid	MinSWRI-Spheroid	MeanSWRI-Spheroid	MaxSWRI-Spheroid	MinLWRI-Spheroid	MeanLWRI-Spheroid	MaxLWRI-Spheroid

226

## 227 3 Methodology

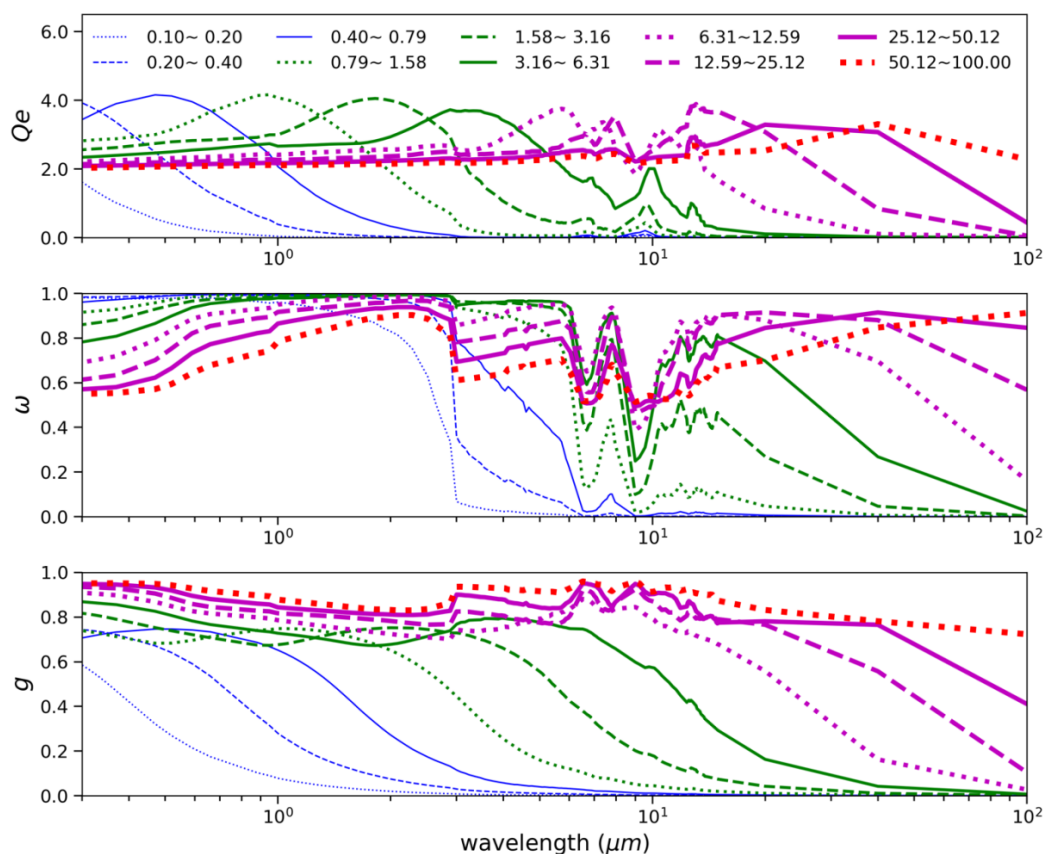
### 228 3.1 Size-resolved dust scattering properties

229 Rapid Radiative Transfer Model (RRTM) (Mlawer et al., 1997) is used to compute both  
230 SW and LW radiative fluxes for both clean (i.e., cloud-free and aerosol-free) and dusty  
231 atmospheres (i.e., free of clouds and non-dust aerosols). RRTM retains reasonable accuracy in  
232 comparison with line-by-line results for single column calculations (Mlawer and Clough, 1998;  
233 Mlawer et al., 1997). It divides the solar spectrum into 14 continuous bands ranging from 0.2 to  
234 12.2  $\mu\text{m}$  and the thermal infrared (3.08–1000  $\mu\text{m}$ ) into 16 bands. We explicitly specify the spectral  
235 DAOD, single scattering albedo ( $\omega$ ), and asymmetry parameter ( $g$ ) of dust aerosols for every band  
236 in the RRTM radiative transfer simulations. In contrast to radiative transfer scheme in most global  
237 models, which do not account for LW scattering, scattering capability is available through the  
238 discrete-ordinate-method radiative transfer (DISORT) in RRTM\_LW (Stamnes et al., 1988).

239 Dust scattering properties (extinction efficiency  $Q_e$ ,  $\omega$  and  $g$ ) depend on several factors  
240 including dust PSD, RI, and dust shape. To account for the impact of dust PSD, we divide dust  
241 diameters into 10 logarithmically spaced size bins. The 10 size bins represent a wide range of dust  
242 geometric diameters (i.e., diameter of a sphere with the same volume) ranging from 0.1  $\mu\text{m}$  to  
243 100  $\mu\text{m}$ . The geometric diameter (hereafter diameter or  $D$ ) range of each size bin is listed in Figure



244 3. For each size bin  $k$ , the spectral scattering properties ( $Qe_k^\lambda$ ,  $\omega_k^\lambda$  and  $g_k^\lambda$ ) are calculated for each  
245 dust model shown in Table 1 and each spectral band. In the calculations of scattering properties  
246 ( $Qe_k^\lambda$ ,  $\omega_k^\lambda$  and  $g_k^\lambda$ ), dust particle number (dN/dD) is assumed to be uniformly distributed within  
247 each size bin. We use the Lorenz–Mie theory code of Wiscombe (1980) to compute the spectral  
248 optical properties of dust particles in the assumption of sphericity. The spectral optical properties  
249 of spheroidal dust particles are derived from the database of Meng et al. (2010). Figure 3 shows  
250  $Qe_k^\lambda$ ,  $\omega_k^\lambda$  and  $g_k^\lambda$  for MeanSWRI-MeanLWRI-Spheroid dust model. In SW, finer dust has a larger  
251  $\omega$  and smaller  $g$ , implying a more effective SW backscattering of finer dust. As a result, finer dust  
252 is expected to have stronger cooling effect (more negative DREE values) at TOA generally. In  
253 LW,  $\frac{Qe_k^{10\mu m}}{Qe_k^{532nm}}$  is generally enhanced as dust size increases, which implies that coarser dust has larger  
254 extinction in LW (optically represented by  $DAOD^{10\mu m}$ ) than finer dust when  $DAOD^{532nm}$  is  
255 constrained by CALIOP retrieval. As a result, larger  $DAOD^{10\mu m}$  will enhance the LW warming  
256 (more positive LW DREE) at TOA of coarser size bins. On the other hand, the increased  $\omega$  and  $g$   
257 of the coarser size bins indicates stronger forward scattering, which reduces the enhancement in  
258 LW warming induced by larger  $DAOD^{10\mu m}$ .



259

260 Figure 3. Spectral scattering properties of each size bin for the MeanSWRI-MeanLWRI-Spheroid dust model. The  
261 scattering properties of each size bin are represented by the corresponding curve indicated in the legend. Each size bin  
262 is defined with respect to dust diameter with unit of micrometers ( $\mu\text{m}$ ).

### 263 3.2 DREE dataset

264 Based on the dust scattering properties shown in Figure 3 and the procedures summarized  
265 in Figure 4, we compute the size-resolved dust DREE for the MeanSWRI-MeanLWRI-Spheroid  
266 dust model in SW and LW. In this section, we focus on demonstrating the method of deriving size-  
267 resolved dust DREE for one dust model, but this method is applicable to all six dust models listed  
268 in Table 1.

269 First, we use RRTM to simulate monthly mean dust DRE from 2007 to 2010 for each  $5^\circ$   
270 (longitude)  $\times$   $2^\circ$  (latitude) grid with CALIOP-based  $DAOD^{532nm}$  exceeding 0.01. The



271  $DAOD^{532nm} \geq 0.01$  threshold ensures most dusty regions over the globe are covered ( see Figure  
272 S1 and Figure S2 in the Supplement) and in the meanwhile balances the computational cost. Dust  
273 DRE are calculated for each size bin using the extinction properties of the corresponding size bin  
274 shown in Figure 3 (denoted as  $DRE_{k,i,j}$ , hereafter  $k$  indicates size bin index and  $(i, j)$  indicates  
275 longitude-latitude grid index, unless specified otherwise). Note that we do not consider dust RI  
276 spatial variation and dust size vertical variation due to the lack of observation-based dust  
277 mineralogy and size estimation on global scale. In  $DRE_{k,i,j}$  calculations, we constrain the monthly  
278 mean dust extinction vertical distributions using the CALIOP-based climatological dataset of Song  
279 et al. (2021). Dust  $DRE_{k,i,j}$  is calculated with respect to  $DAOD_{i,j}^{532nm}$  from CALIOP-based DAOD  
280 climatology. The atmospheric profiles such as water vapor ( $H_2O$ ), ozone ( $O_3$ ) and temperature  
281 ( $T_{atm}$ ) vertical profiles of 72 levels are from 3-hourly MERRA2 assimilated meteorological fields  
282 data (Gelaro et al., 2017). We combine the 1-hourly surface albedo for visible beam from  
283 MERRA2 radiation diagnostics with the instantaneous spectral surface albedo from the integrated  
284 CALIPSO, Cloud-Sat, CERES, and MODIS merged product (CCCM) (Kato et al., 2011) to get  
285 time-dependent spectral surface albedo. Surface temperature is obtained from 1-hourly MERRA2  
286 radiation diagnostics data. The atmospheric and surface properties are all aggregated to monthly  
287 mean values at eight UTC times: 0:30, 3:30, 6:30, 9:30, 12:30, 15:30, 18:30, 21:30 to obtain  
288 monthly-mean diurnal cycle for radiative transfer simulations. Considering  $DRE^{SW}$  strongly  
289 depends on solar zenith angle (SZA), we calculate  $DRE^{SW}$  for every 1 hour using the corresponding  
290 hourly SZA in midmonth day. As a result, every three SZA share the same atmospheric and surface  
291 properties in  $DRE^{SW}$  calculations due to their different temporal resolution.

292 Table 2 List of definitions of variables and their indices.

Variable	Definition
k	size bin index
i, j	longitude-latitude grid index



$t$	8 UTC times with 3-hour interval (i.e., 0:30, 3:30, 6:30, 9:30, 12:30, 15:30, 18:30, 21:30)
$tt$	24 UTC times with 1-hour interval
$day^{mm}$	The midmonth day of the month
$\overline{R(t), H_2O(t), O_3(t), CO_2(t), T_{atm}(t)}$	3-hourly monthly mean surface albedo and vertical profile of water vapor, ozone, carbon dioxide and atmospheric temperature
$\zeta_d$	dust properties such as DAOD, dust extinction vertical profile and scattering properties
$\overline{{}_{1h}DRE_{k,i,j}^{SW}(tt)}$	1-hourly monthly mean $DRE^{SW}$ (i.e., monthly mean $DRE^{SW}$ at each of 24 UTC times) of $k^{th}$ size bin and ( $i^{th}, j^{th}$ ) grid
$\overline{{}_{3h}DRE_{k,i,j}^{LW}(t)}$	3-hourly monthly mean $DRE^{LW}$ (i.e., monthly mean $DRE^{LW}$ at each of 8 UTC times) of $k^{th}$ size bin and ( $i^{th}, j^{th}$ ) grid
$\overline{DRE_{k,i,j}^{SW}, DRE_{k,i,j}^{LW}}$	The monthly and diurnally mean dust $DRE^{SW}$ and $DRE^{LW}$ of $k^{th}$ size bin and in ( $i^{th}, j^{th}$ ) grid
$\overline{DRE_{k,i,j}}$	The monthly and diurnally mean dust $DRE^{SW}$ and $DRE^{LW}$ of $k^{th}$ size bin and ( $i^{th}, j^{th}$ ) grid
$\overline{DAOD_{i,j}^{532nm}}$	The monthly mean dust optical depth at 532nm of ( $i^{th}, j^{th}$ ) grid

293

294 The definitions of variables and indices used to derive size-resolved dust DREE dataset are  
 295 summarized in Table 2. Eq. (1) shows the way of deriving 1-hourly monthly mean  $DRE^{SW}$ .

$$\overline{{}_{1h}DRE_{k,i,j}^{SW}(tt)} = DRE_{k,i,j}^{SW}(\overline{R(t)}, \overline{H_2O(t)}, \overline{O_3(t)}, \overline{CO_2(t)}, \zeta_d, SZA(day^{mm}, tt)), \quad (1)$$

296 where ‘ $t$ ’ indicates 8 UTC times with 3-hour interval. ‘ $tt$ ’ indicates 24 UTC times with 1-hour  
 297 interval. ‘ $day^{mm}$ ’ indicates the midmonth day of the month, and ‘ $\overline{R(t)}, \overline{H_2O(t)}, \overline{O_3(t)}, \overline{CO_2(t)}$ ’  
 298 represent 3-hourly monthly mean surface albedo and vertical profile of water vapor, ozone, carbon  
 299 dioxide, respectively. The temporal resolution inconsistency of SZA as well as atmospheric and  
 300 surface properties requires every three SZA share the same atmospheric and surface properties in  
 301 the calculations. ‘ $\zeta_d$ ’ represents dust properties such as DAOD, dust extinction vertical profile and  
 302 scattering properties which are independent of UTC time in our calculations. Dust extinction  
 303 vertical profile is interpolated to the 72 levels in consistency with vertical profiles of water vapor,  
 304 ozone and temperature from MERRA2.

305 Eq. (2) shows the way of deriving 3-hourly monthly mean  $DRE^{LW}$ . Surface emissivity (‘ $E$ ’)  
 306 is obtained from Huang et al. (2016), which contains monthly mean spectral surface emissivity  
 307 with 0.5-degree spatial resolution.  $\overline{T_{atm}(t)}$  represents 3-hourly monthly mean vertical profile of



308 atmospheric temperature. With the aid of the 3-hourly monthly mean atmospheric properties,  
 309 monthly mean  $DRE^{LW}$  is calculated for every 3 hours.

$$\overline{{}_{3h}DRE_{k,i,j}^{LW}(t)} = DRE_{k,i,j}^{LW}(\overline{E}, \overline{H_2O(t)}, \overline{O_3(t)}, \overline{CO_2(t)}, \overline{T_{atm}(t)}, \overline{\zeta_d}) \quad (2)$$

310 Then the 1-hourly monthly mean dust  $DRE^{SW}$  ( $\overline{{}_{1h}DRE_{k,i,j}^{SW}(tt)}$ ) derived from Eq. (1) is  
 311 averaged diurnally (over 24 points) to get the monthly and diurnally mean dust  $DRE^{SW}$  ( $\overline{DRE_{k,i,j}^{SW}}$ )  
 312 as indicated by Eq. (3). Similarly, the 3-hourly monthly mean  $DRE^{LW}$  ( $\overline{{}_{3h}DRE_{k,i,j}^{LW}(t)}$ ) derived from  
 313 Eq. (2) is averaged diurnally (over 8 points) to get the monthly and diurnally mean dust  $DRE^{LW}$   
 314 ( $\overline{DRE_{k,i,j}^{LW}}$ ) as indicated by Eq. (4). The method described by Eq. (1) - Eq. (4) will be referred to as  
 315 the ‘conventional’ method of calculating monthly mean dust DRE in Section 4.

$$\overline{DRE_{k,i,j}^{SW}} = \frac{\sum_{tt} \overline{{}_{1h}DRE_{k,i,j}^{SW}(tt)}}{\sum tt} \quad (3)$$

$$\overline{DRE_{k,i,j}^{LW}} = \frac{\sum_t \overline{{}_{3h}DRE_{k,i,j}^{LW}(t)}}{\sum t} \quad (4)$$

316 Based on the monthly mean size-resolved dust  $DRE^{SW}$  ( $\overline{DRE_{k,i,j}^{SW}}$ ) and  $DRE^{LW}$  ( $\overline{DRE_{k,i,j}^{LW}}$ ), we  
 317 derive the monthly mean size-resolved dust DREE ( $\overline{DREE_{k,i,j}}$ ) using Eq. (5) for SW and LW  
 318 respectively. Note that the monthly mean size-resolved dust DREE ( $\overline{DREE_{k,i,j}}$ ) is calculated by  
 319 dividing by monthly mean  $DAOD^{532nm}$  since the size-resolved  $\overline{DRE_{k,i,j}}$  was initially derived with  
 320 respect to monthly mean  $DAOD^{532nm}$ .

$$\overline{DREE_{k,i,j}^{SW \text{ or } LW}} = \frac{\overline{DRE_{k,i,j}^{SW \text{ or } LW}}}{\overline{DAOD_{i,j}^{532nm}}} \quad (5)$$

321 Finally, we average the monthly mean size-resolved dust DREE ( $\overline{DREE_{k,i,j}}$ ) over 4 years  
 322 to get monthly mean size-resolved dust DREE datasets in addition to the associated interannual  
 323 standard deviation (std). The std indicates the DREE uncertainty caused by interannual variation

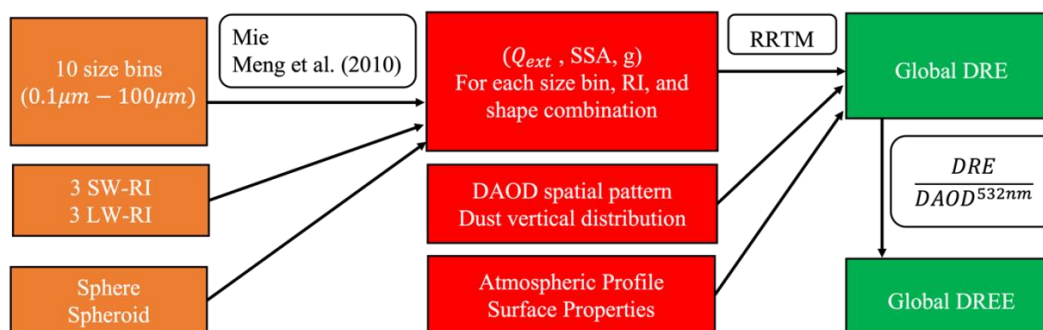


324 of monthly mean atmospheric and surface properties as well as dust vertical distribution. Finally,  
325 the dataset developed in this study contains monthly mean size-resolved dust DREE and its  
326 associated interannual std at TOA and surface with dimension of 10 bins, 12 months, 90 latitudes,  
327 72 longitudes for each of six dust models in SW and LW respectively. Figure S1 and Figure S2 in  
328 the Supplement demonstrate the global distribution of the monthly mean size-resolved DREE<sup>SW</sup>  
329 and DREE<sup>LW</sup> at TOA for June.

330 It is important to note that dust DREE of each grid cell rarely depends on the DAOD  
331 because dust DRE is approximately linear with DAOD (Satheesh and Ramanathan, 2000).  
332 Therefore, the choose of CALIOP- or MODIS-based DAOD climatology to derive the global  
333 ( $5^\circ \times 2^\circ$ ) size-resolved DREE dataset will not lead to large difference. In other words, the size-  
334 resolved DREE dataset is rarely related to the robustness of the DAOD used in the derivation  
335 process. We select CALIOP-based DAOD to derive the size-resolved dust DREE dataset because  
336 that the CALIOP-based dust climatology contains dust vertical distribution, which is especially  
337 important for obtaining LW DREE. Nevertheless, using CALIOP-based dust retrieval to derive  
338 size-resolved dust DREE dataset has several limitations: (1) The size-resolved dust DREE dataset  
339 may miss some regions with tenuous dust layers that below the CALIOP sensitivity. (2) The LW  
340 DREE is related to the quality of dust vertical distribution retrieval. By contrast, dust DRE highly  
341 depends on DAOD, therefore we will use different DAOD climatological datasets retrieved from  
342 different sensors (i.e., CALIOP and MODIS) to investigate global dust DRE in section 5.2.  
343 Furthermore, even though dust DREE of each grid cell is rarely related to DAOD, regional or  
344 global mean dust DREE will depend on the DAOD spatial distribution (i.e., DAOD 2D distribution)  
345 in the region of interest (see details in section 5.2).

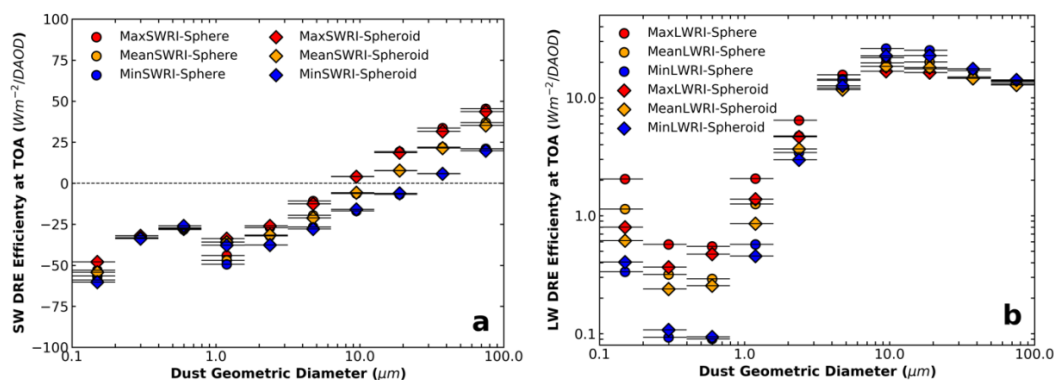


346           Based on the monthly mean size-resolved dust DREE datasets derived above, we further  
347 calculate globally annual mean size-resolved dust  $DREE^{SW}$  and  $DREE^{LW}$  at TOA and surface for  
348 the six dust models (Figure 5). As discussed above, the global mean dust DREEs depends on the  
349 DAOD spatial distribution, the global mean dust DREEs shown in Figure 5 is based on CALIOP-  
350 based DAOD spatial distribution from Song et al. (2021). Generally smaller bins cause stronger  
351 cooling in SW and less warming in LW, which is consistent with our discussions in 3.1. This  
352 observationally informed globally annual mean size-resolved dust DREE is also consistent with  
353 the model-simulated results shown in supplementary Figure S3 in Kok et al. (2017) in terms of the  
354 variation trend of DREE with respect to dust size. Moreover, our study explicitly shows the  
355 sensitivity of dust DREE to dust RI and dust shape. For example, Figure 5 shows that  $DREE^{SW}$  is  
356 strongly sensitive to dust RI as  $DREE^{SW}$  of different dust RI is widely separated. Depending on  
357 dust RI,  $DREE^{SW}$  switches from cooling effect (negative value) to warming effect (positive value)  
358 at different size bins. More absorptive dust starts to warm the Earth system in SW at smaller dust  
359 size, and vice versa. In addition, our results suggest that  $DREE^{SW}$  is generally not sensitive to dust  
360 shape. Specifically, dust shape is not important for  $DREE^{SW}$  in most size bins, while it is important  
361 in the fourth size bin ( $D: 0.79\mu m \sim 1.58\mu m$ ) with  $DREE^{SW}$  of spheroidal dust obviously higher  
362 (less negative) than spherical dust. In the  $DREE^{LW}$ , dust shape is almost as important as RI for  
363 several size bins.



364

365 Figure 4. Schematic of the methodology used to derive size-resolved dust DREE dataset. Orange boxes denote dust  
 366 models used to calculate dust scattering properties. Red boxes denote inputs for RRTM. Green boxes denote outputs  
 367 from RRTM.



368

369 Figure 5. Globally annual mean size-resolved dust DREE in SW (a) and LW (b) for six dust models (six markers).  
 370 Horizontal bars indicate the dust diameter range of each size bin. Note: LW DREE is on a logarithm scale; in contrast to  
 371 global model simulations, we consider dust LW scattering in LW DRE Efficiency calculations.

372 Our size-resolved dust DREE dataset is unique in many aspects: First, our DREE dataset  
 373 is derived based on CALIOP-based dust 3D distribution. Size-resolved DREE is derived for all  
 374 grids with CALIOP-based DAOD  $\geq 0.01$ . Second, our size-resolved DREE dataset covers a wide  
 375 range of dust diameters, specifically, they include dust DREE for ten dust diameter size bins  
 376 ranging from  $0.1 \mu\text{m}$  to  $100 \mu\text{m}$ . This is challenging, if not impossible, to obtain from global  
 377 models because these models generally simulate dust particles with diameter only up to  $20 \mu\text{m}$  and  
 378 coarse dust particles in models deposit quickly and could not be sustained to the remote transport  
 379 regions (Huneus et al., 2011; Adebisi and Kok, 2020) where coarse particles have been observed



380 by in-situ measurements (Weinzierl et al., 2017). As a result, our size-resolved DREE dataset  
381 achieves a wide spatial coverage for a large range of dust size. This is critical for investigating  
382 impacts of coarse dust and even giant dust particles on dust DRE on both regional and global scales.  
383 Third, considering that the dust vertical distribution is important for quantifying  $DRE^{LW}$ , we  
384 constrain dust vertical distribution using CALIOP-based dust retrievals in  $DRE^{LW}$  computation.  
385 Fourth, our size-resolved dust DREE dataset accounts for dust LW scattering in  $DRE^{LW}$   
386 calculations since scattering capability is available through the DISORT in RRTM\_LW (Stamnes  
387 et al., 1988). Dufresne et al., (2002) suggests that dust LW scattering enhances dust LW warming  
388 effect at TOA by a factor of up to 50%. However, dust LW scattering is generally not considered  
389 in most global models. Therefore, many previous studies artificially account for dust LW scattering  
390 by increasing the radiative perturbation due to LW absorption by a certain fraction. For example,  
391 Kok et al. (2017) accounts for LW scattering by artificially augmenting  $DRE^{LW}$  by 23% and Di  
392 Biagio et al. (2020) augmented  $DRE^{LW}$  by 50%.

393 On the other hand, our size-resolved dust DREE dataset has several limitations. First,  
394 possible vertical variations in dust particle size are not accounted for in our calculation. The entire  
395 dust-loading column is assumed to have the same dust size distribution. Second, we do not  
396 explicitly account for spatial variation of dust RI, in other words, dust RI is assumed to be globally  
397 uniform. This uncertainty is assessed through the sensitivity tests of DREE to dust RI using three  
398 sets of state-of-the-art dust RI based on laboratory measurement of 19 dust samples all over the  
399 world. Third, dust 3D distribution in the DREE calculation is constrained by CALIOP observations.  
400 The limits on the sensitivity of CALIOP will affect the 3D distribution of dust in our calculation.  
401 Fourth, we account for dust nonsphericity by using spheroidal shape model. This shape can't  
402 perfectly represent the highly irregular shape and roughness of real dust. In addition, several



403 studies suggest that dust non-sphericity is underestimated by the spheroidal shape model (Huang  
404 et al., 2020). The spheroidal shape model assumption thus might produce systematic errors.

405 Overall, the size-resolved dust DREE dataset is useful in many dust-related studies. First,  
406 with our size-resolved dust DREE dataset, dust DRE could be calculated efficiently for any DAOD  
407 magnitude, DAOD spatial pattern and any dust PSD for any regions or the globe (see details in  
408 Section 4.1). Second, our size-resolved DREE dataset is derived for different RI and different dust  
409 shapes respectively. As a result, we could estimate dust DRE uncertainty coming from DAOD,  
410 PSD, RI, and shape separately to better understand major uncertainty sources in dust DRE  
411 estimations. Third, our size-resolved DREE dataset could be used to evaluate model simulated  
412 DREE for each size bin.

## 413 **4 DRE calculation methodology and its validation**

### 414 **4.1 DRE calculation based on DREE dataset**

415 With the size-resolved dust DREE dataset derived in section 3.2, DRE of dust with any  
416 PSD and DAOD could be computed very efficiently without performing radiative transfer  
417 simulations as we do in *conventional* method. This section introduces the methodology of applying  
418 the size-resolved DREE dataset to calculate DRE of dust with any PSD and DAOD.

419 DRE of full size range of dust can be expressed as the sum of DRE from each size bin  
420 ( $DRE_k$ ). Dust  $DRE_k$  is approximated to be linearly proportional to DAOD of  $k^{th}$  size bin ( $DAOD_k$ )  
421 (Satheesh and Ramanathan, 2000). The similar concept of calculating dust DRE has been used in  
422 previous studies e.g., Kok et al. (2017). Eq. (6) shows the process of computing dust DRE using  
423 the size-resolved DREE dataset.

$$DRE = \sum_k DRE_k = \sum_k DREE_k \times DAOD_k = \sum_k DREE_k \times f_k \times DAOD, \quad (6)$$



424 where  $DRE$  represents dust DRE induced by full size range of dust with optical depth of  $DAOD$ .  
425  $f_k$  is the fraction of the DAOD contributed by the  $k^{th}$  size bin.

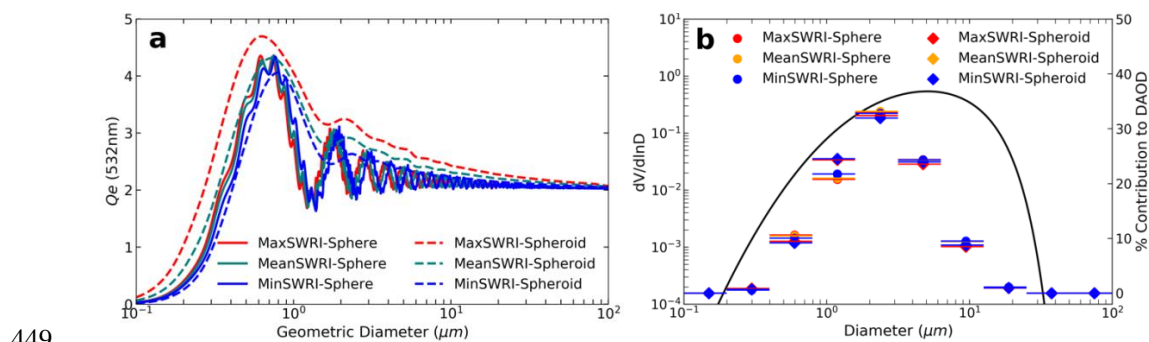
426 Each variable in Eq. (6) can be obtained or derived from datasets developed in this study  
427 and other studies. For example, the size-resolved DREE dataset ( $DREE_{k,i,j}$ ) derived in this study  
428 is essential for utilizing this efficient and novel DRE calculation method. DAOD can be obtained  
429 from CALIOP-based or MODIS-based DAOD climatological datasets (Song et al., 2021).  $f_k$  can  
430 be derived from dust extinction efficiency ( $Qe$ ), the geometric cross-sectional area ( $A$ ) and dust  
431 PSD ( $dN/dD$ ) based on Eq. (7).

$$f_k \equiv \frac{DAOD_k}{DAOD} = \frac{\int_{D^{k-}}^{D^{k+}} Qe^{532nm}(D)A(D) \frac{dN}{dD} dD}{\int_0^{D^{max}} Qe^{532nm}(D)A(D) \frac{dN}{dD} dD} \quad (7)$$

432  $Qe$  is defined according to  $Qe \equiv \frac{\sigma_e}{A}$ , where  $\sigma_e$  is extinction cross section, the geometric  
433 cross-sectional area of the particle ( $A$ ) can be expressed as  $A = \pi r^2$ . Under the assumption of  
434 spherical dust particle,  $r$  is the radius. Under the assumption of spheroidal dust particle, Vouk  
435 (1948) shows that the average projected area of a convex body (e.g., spheroidal particle) is  $A =$   
436  $\pi r^2$ , where  $r$  is the radius of a surface area-equivalent sphere. The average is taken over all  
437 possible orientations in space, which is consistent with our assumption of randomly oriented dust  
438 particles in the atmosphere.  $Qe^{532nm}(D)$  for the six dust models are shown in Figure 6 (a), they  
439 all converge to 2 as the dust diameter becomes much larger than the wavelength, which is  
440 consistent with the principle of geometric optics (van de Hulst, 1957). By contrast,  $Q_e^{550nm}(D)$  of  
441 non-spherical dust in Kok et al. (2017) has a much larger value than spherical dust for dust  $D \geq$   
442  $1\mu m$  (see their Figure 1(b)). This discrepancy is probably due to the different  $Q_e$  definitions used  
443 in the two studies. Kok et al. (2017) defined  $Q_e$  as dust extinction per unit cross section of volume-  
444 equivalent sphere. Figure 6 (b) shows that  $f_k$  of a specific PSD is not sensitive to dust RI and dust



445 shape, this is also suggested by the similar  $Qe^{532nm}$  v.s. geometric diameter ( $D$ ) trends of the six  
446 dust models shown in Figure 6 (a). In contrast,  $f_4$  (i.e.,  $f_k$  for the fourth size bin with  $D$  ranging  
447 from  $0.79\mu m$  to  $1.58\mu m$ ) is more sensitive to dust shape than other size bins, this is in line with  
448 the larger difference in  $Qe^{532nm}$  with shape shown in Figure 6 (a).

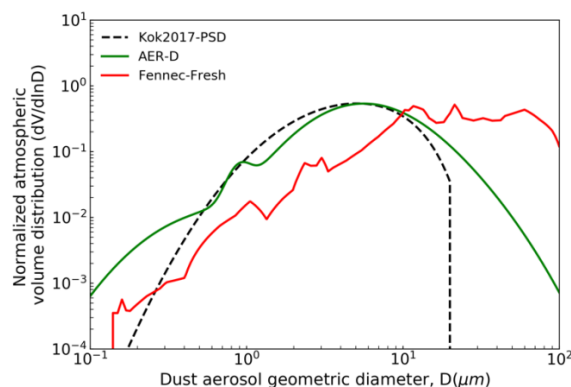


449  
450 Figure 6. (a) Dust extinction efficiency ( $Q_e$ ) at 532nm for six dust models. (b) The colorful bars represent  $f_k$   
451 calculated for six dust models based on a specific dust PSD ( $dV/d\ln D$ ) indicated by black curve. Note,  $f_k$  is not  
452 sensitive to different dust models such as dust RI and dust shape.

453 In summary, the size-resolved dust DREE dataset provides an efficient way to compute  
454 DRE for any dust PSD and any DAOD by using Eq. (6) and Eq. (7). To distinguish from the  
455 *conventional* method introduced in section 3.2, this method of calculating dust DRE based on size-  
456 resolved DREE dataset is referred to as ‘*DREE-integration*’ method.

#### 457 4.2 Validation of DRE calculation methodology

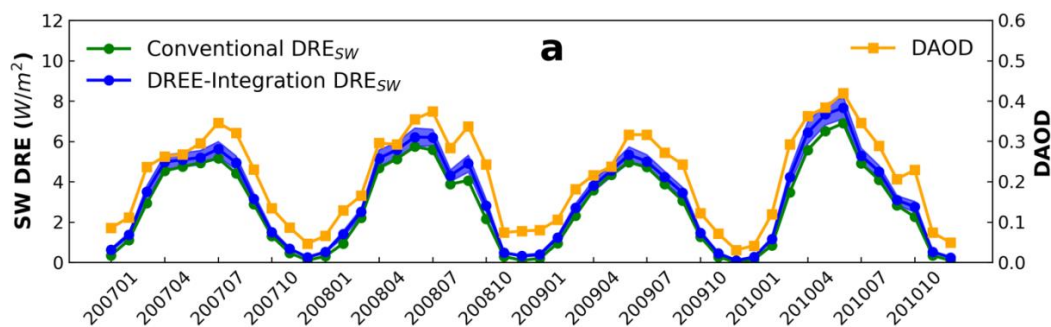
458 In this section, we select the Sahara Desert ( $14^\circ N$ - $30^\circ N$ ,  $15^\circ W$ - $30^\circ E$ ) to validate the  
459 *DREE-integration* method. We choose MeanSWRI-MeanLWRI-Spheroid dust model and Fennec-  
460 Fresh dust PSD (see red curve in Figure 7) measured within 12h of dust uplift in remote Sahara  
461 locations by Fennec field campaign to represent microphysical properties of Saharan dust (Ryder  
462 et al., 2013a, b). Monthly mean DAOD is from CALIOP-based DAOD climatology.



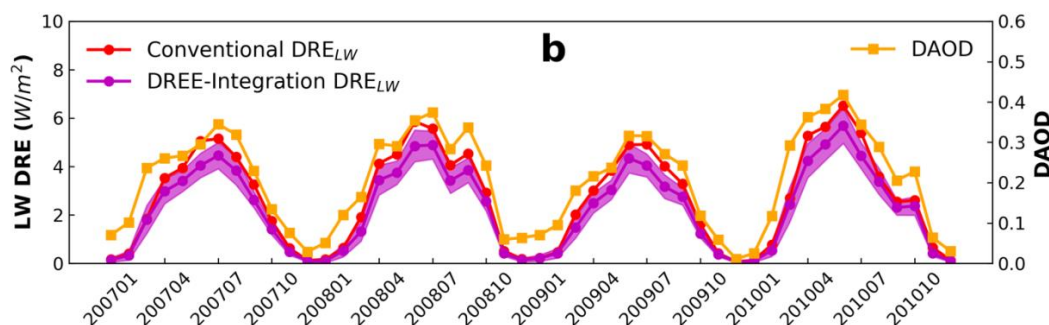
463

464 Figure 7. Normalized atmospheric dust volume distribution ( $dV/d\ln D$ ) described in Table 5 (Kok et al., 2017; Ryder  
465 et al., 2013a; b; 2018; 2019).

466 Figure 8 shows the comparison of 4-year (2007-2010) monthly mean dust DRE between  
467 the *Conventional* and *DREE-integration* method. In *Conventional* DRE calculation, dust scattering  
468 properties ( $Q_e$ ,  $\omega$  and  $g$ ) are calculated based on the Fennec-Fresh PSD and then used to calculate  
469 monthly mean dust DRE from 2007 to 2010 with RRTM as described in Section 3.2 (Eq. 1 – Eq.  
470 4). While the *DREE-integration* method is based on the monthly mean size-resolved *DREE* dataset  
471 derived based on 4-year (2007-2010) data as described in Section 4.1 (Eq. 6 – Eq. 7). The excellent  
472 agreement in monthly mean dust DRE between two methods validates the *DREE-integration* DRE  
473 calculation methodology.



474



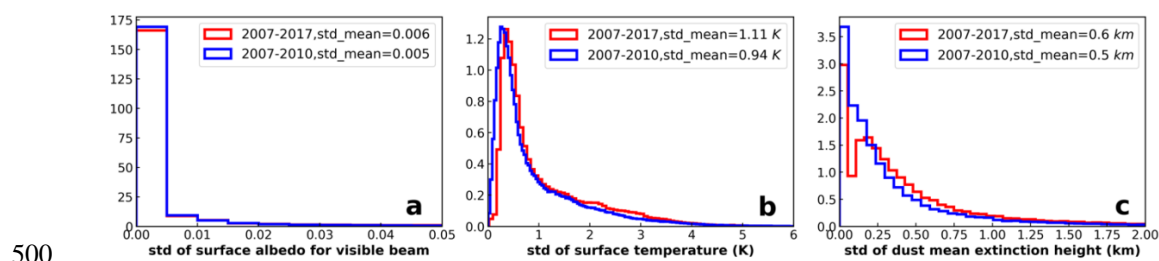
475

476 Figure 8. Monthly mean dust  $DRE^{SW}$  (a) and  $DRE^{LW}$  (b) comparison between *Conventional* and *DREE-integration*  
 477 calculation from 2007 to 2010 over Sahara Desert. Shaded area along *DREE-integration* DRE indicates the one  
 478 standard deviation caused by the atmospheric and surface variations as well as dust vertical distribution variation  
 479 within the four years. Orange curves indicate CALIOP-based monthly mean DAOD. The variation of dust DRE match  
 480 well with DAOD variation.

481 The shaded-area associated with DREE-integration DRE corresponds to the one standard  
 482 deviation of DREE caused by the 4-year (2007-2010) interannual variation of factors except dust  
 483 microphysical properties such as monthly mean atmospheric and surface properties as well as dust  
 484 vertical distributions (hereafter those factors is referred to as non-dust-factors for short). The  
 485 narrow shaded-area along DREE-integration DRE suggests non-dust-factors cause very small  
 486 uncertainty in dust DRE estimations. However, the small effects of 4-year interannual variation of  
 487 non-dust-factors may not necessarily be representative due to the limited number of years  
 488 considered. Section 2.1 discusses in detail for the reason of choosing 2007-2010 to derive size-  
 489 resolved DREE dataset. To check the representative of 4-year interannual variation for non-dust-  
 490 factors, we compare the 4-year (2007-2010) and 10-year (2007-2017) interannual standard  
 491 deviation (std) of monthly mean non-dust-factors (e.g., surface albedo, surface temperature and  
 492 dust vertical distribution) in Figure 9. To evaluate the interannual variation of dust vertical  
 493 distribution, we define dust mean extinction height ( $Z_\alpha$ ) referring to Koffi et al. (2012) as  $Z_\alpha =$   
 494  $\frac{\sum_{i=1}^n \beta_{ext,i} \times Z_i}{\sum_{i=1}^n \beta_{ext,i}}$ , where  $\beta_{ext,i}$  is the dust extinction coefficient at 532nm at level  $i$ , and  $Z_i$  is the altitude  
 495 of level  $i$ . Nevertheless the 10-year std is slightly larger than 4-year std, they are both close to zero



496 and on the same order of magnitude. As such, even though our monthly mean size-resolved DREE  
497 dataset is derived from 4-year (2007-2010) data, they could be used to represent DREE and  
498 calculate DRE for other years considering the small sensitivity of monthly mean dust DRE to  
499 interannual variation of non-dust-factors.



501 Figure 9. Probability density function (PDF) of 4-year and 10-year interannual standard deviation (std) in monthly  
502 mean (a) surface albedo, (b) surface temperature, and (c) dust mean extinction height. The PSD analyses include  
503 interannual std in 12 months and all  $5^\circ$  (longitude)  $\times$   $2^\circ$  (latitude) grid cells over the world and their mean values are  
504 indicated as 'std\_mean' on each figure.

## 505 **5 Regional and global dust DRE based on size-resolved DREE dataset**

506 After the validation of *DREE-integration* method in Section 4, we use the *DREE-integration*  
507 method to calculate regional and global dust DRE in this section. There are three main objectives  
508 in this section: (1) the most important objective throughout this section is to demonstrate the  
509 usefulness of the size-resolved DREE dataset for calculating regional and global dust DRE for any  
510 given dust PSD; (2) the second objective is to validate the size-resolved DREE dataset by  
511 comparing with regional dust DREE reported by field studies based on satellite and ground-based  
512 observations (section 5.1); (3) the third objective to assess the sensitivity of dust DRE to DAOD  
513 spatial pattern (section 5.2) as well as dust microphysical properties such as dust PSD, RI and  
514 shape (section 5.3).

### 515 **5.1 Comparison with observation-based regional dust DREE**

516 Table 3 shows the comparison of our calculations of clear-sky regional mean SW and LW  
517 DREE with those reported by field studies based on satellite and ground-based observations. We



518 first calculated regional mean dust DRE using the *DREE-integration* method, then divided by the  
519 corresponding regional mean DAOD to get regional mean DREE, and then compared this with  
520 observation-based results from previous studies. Comparing DREE allows eliminating differences  
521 due to the variation in regional dust loading, optically represented by DAOD.

522 Knowledge of regional dust PSD is necessary for estimating dust DRE regionally. There are  
523 several in-situ measurements of dust PSD over Sahara and tropical eastern Atlantic. The state-of-  
524 the art airborne observations of Saharan dust from the Fennec field campaign (Fennec-Fresh) and  
525 transported Saharan dust over tropical eastern Atlantic within Saharan Air Layer (SAL) from both  
526 AER-D and Fennec fieldwork campaigns are adopted (Ryder et al., 2013 a, b, 2018, 2019) (see  
527 Figure 7). Both campaigns include giant dust particles, measuring up to  $100\mu\text{m}$  diameter for AER-  
528 D and up to  $300\mu\text{m}$  for Fennec. The wide coverage of dust diameter in our size-resolved DREE  
529 dataset allows for dust DRE calculations for giant dust up to  $100\mu\text{m}$  over both dust source and  
530 transported regions where giant particles are observed in those campaigns. This is an advantage of  
531 our size-resolved DREE dataset compared to modeled dust DREE, because climate models  
532 generally cut off dust diameter at  $20\mu\text{m}$  and could not sustain coarse dust to remote transport  
533 regions due to several missing mechanisms in models (Van Der Does et al., 2018; Drakaki et al.,  
534 2022; Meng et al., 2022).

535 The Fennec-Fresh dust PSD includes measurements within 12h of dust uplift in remote  
536 Sahara locations. It is used to calculate dust DRE for Saharan dust in this section. In reality, dust  
537 over the wide Sahara Desert region ( $15\text{N}\sim 30\text{N}$ ,  $10\text{W}\sim 30\text{E}$ ) is not all lifted within 12h, so using  
538 Fennec-Fresh to represent dust PSD over the wide Sahara Desert could bias dust size coarse, which  
539 could partially explain the warm bias in our  $\text{DREE}^{\text{SW}}$  estimation over the Sahara Desert compared  
540 to the satellite-based result. Over the tropical Atlantic, both AER-D and Fennec-SAL measured



541 PSD are used to assess the sensitivity of dust DREE to dust PSD. In addition, dust DRE is  
 542 calculated for three dust RIs to evaluate the sensitivity of dust DREE to dust RI as shown in Table  
 543 3. Generally, our dust DREE estimations achieve good agreement with observation-based dust  
 544 DREE. However, there is a significant uncertainty caused by dust RI in DREE, especially for SW.  
 545 In addition, DRE comparisons between AER-D and Fennec-SAL over the Tropical Atlantic  
 546 suggests that in-situ measured dust PSD uncertainty leads to a large uncertainty in regional DREE  
 547 in both SW and LW.

548 Based on the regional DREE study with the state-of-the art RI and PSD, we found DREE<sup>SW</sup>  
 549 uncertainty could come from both dust RI and dust PSD, while DRE<sup>LW</sup> uncertainty is mainly from  
 550 dust PSD.

551 Table 3. Comparison of our DREE estimations for different PSD and RI with Clear-Sky regional SW and LW dust  
 552 DREE reported by field studies based on satellite and ground-based observations. Specifically, we calculated regional  
 553 dust DREE for different RI (Min, Mean, Max) and different PSD (AER-D and Fennec-SAL for Tropical Atlantic) and  
 554 then compare with observation-based results from previous studies. Note, spheroidal dust shape is assumed in our  
 555 DREE-integration DRE calculations.

Shortwave Spectral Range							
Region	Season	Level	Satellite- Based DREE <sup>SW</sup>	This study			
				DREE <sup>SW</sup>			PSD
				Min RI	Mean RI	Max RI	
Sahara Desert <sup>(a)</sup> (15N~30N, 10W~30E)	JJA	TOA	0	2.8	16.0	26.6	Fennec-Fresh
Ilorin <sup>(f)</sup> , Nigeria (8.5N, 4.7E)	Annual	TOA	-15 ~ -35	-28.3	-24.1	-19.9	AER-D
				-23.4	-17.7	-12.9	Fennec-SAL
		Surface	-49 ~ -75	-43.1	-51.7	-59.3	AER-D
				-46.0	-57.1	-66.0	Fennec-SAL
Cape Verde <sup>(f)</sup> (16.7N, 22.9W)	Annual	TOA	-36 ~ -48	-42.3	-38.0	-33.7	AER-D
				-36.6	-30.8	-26.0	Fennec-SAL
		Surface	-68 ~ -90	-59.6	-68.7	-77.7	AER-D
				-61.5	-74.6	-85.3	Fennec-SAL
Tropical Atlantic <sup>(b)</sup> (10N~30N, 20W~45W)	JJA	TOA	-28	-44.6	-39.9	-35.3	AER-D
				-38.4	-32.1	-27.0	Fennec-SAL
		Surface	-82.1	-61.1	-71.9	-81.7	AER-D
				-64.4	-78.5	-90.0	Fennec-SAL
Tropical Atlantic <sup>(c)</sup> (15N~25N, 15W~45W)	JJA	TOA	-35	-41.2	-36.3	-31.5	AER-D
				-35.1	-28.5	-23.1	Fennec-SAL
		Surface	-65	-57.9	-68.6	-78.1	AER-D
				-61.2	-75.1	-86.3	Fennec-SAL
Longwave Spectral Range							



Region	Season	Level	Satellite- Based DREE <sup>LW</sup>	This study			PSD
				DREE <sup>LW</sup>			
				Min RI	Mean RI	Max RI	
Sahara Desert <sup>(a)</sup> (15N~30N, 10W~30E)	JJA	TOA	11~26	13.4	11.8	11.4	Fennec-Fresh
North Africa <sup>(d-e)</sup> (15N~35N, 18W~40E)	JJA	TOA	15~22	14.4	12.8	12.4	Fennec-Fresh
Tropical Atlantic <sup>(b)</sup> (10N~30N, 20W~45W)	JJA	TOA	10.5	8.2	8.1	8.5	AER-D
				13.1	11.8	11.6	Fennec-SAL
Cape Verde <sup>(g)</sup> (16.7N, 22.9W)	Sept	Surface	16	8.0	11.8	15.1	AER-D
				13.0	17.0	19.8	Fennec-SAL

(a) Patadia et al. (2009). (b) Song et al. (2018). (c) Li et al. (2004). (d) Zhang and Christopher (2003). (e) Brindley and Russell (2009). (f) Zhou et al. (2005). (g) Hansell et al. (2010)

556

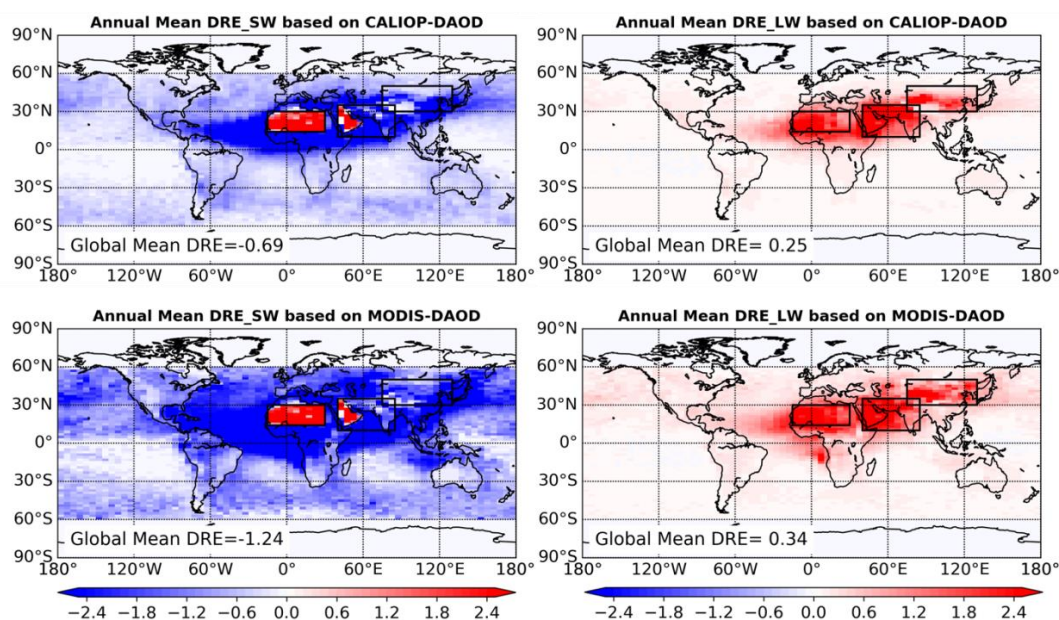
## 557 5.2 Global dust clear-sky DRE based on different DAOD climatology

558 The DAOD is the most important factor in determining dust DRE. As illustrated in Song et  
 559 al. (2021), the DAOD retrieved from different satellite sensors have a large difference in terms of  
 560 magnitude and spatial distribution. To evaluate how the current DAOD uncertainty affects dust  
 561 DRE estimations, the global dust DRE computed based on monthly mean DAOD climatology  
 562 retrieved from CALIOP observations and MODIS observations are compared in this section. To  
 563 separate the effect of DAOD from other factors, we use the same dust PSD, RI and shape in the  
 564 two sets of dust DRE calculations in this section. Specifically, we use the Fennec-Fresh PSD for  
 565 three major dust source regions (i.e., Sahara (14-30°N, 15°W-30°E), Middle East (10-35°N, 40-  
 566 85°E) and eastern Asia (30-50°N, 75-130°E), they are indicated by three black boxes in Figure 10)  
 567 and use AER-D PSD for other regions (hereafter Campaign-PSD, see Table 5). The MeanSWRI-  
 568 MeanLWRI-Spheroid dust model described in Table 1 is used to represent dust RI and shape.

569 The two DAOD climatological datasets result in distinct dust DRE spatial pattern as shown  
 570 in Figure 10, which is consistent with the DAOD spatial patterns shown in Figure 1 suggesting  
 571 CALIOP DAOD is more concentrated over ‘dust belt’ regions than MODIS DAOD. The global  
 572 mean dust DRE<sup>SW</sup>, DRE<sup>LW</sup> and DRE<sup>NET</sup> based on the two DAOD climatology are significantly



573 different (Table 4), which is mainly caused by two factors. The first is the difference in DAOD  
574 magnitude. The CALIOP-based global mean DAOD is 0.032, while MODIS-based is 0.047. The  
575 other factor is the difference in DAOD spatial pattern. After we scale dust DRE to the same global  
576 mean DAOD ( $\overline{DAOD} = 0.03$ ) to eliminate the effect of DAOD magnitude difference (values in  
577 parentheses in Table 4), the  $DRE^{SW}$  difference reduced from  $0.55 \text{ W m}^{-2}$  ( $-0.69$  vs.  $-1.24 \text{ W m}^{-2}$ )  
578 to  $0.15 \text{ W m}^{-2}$  ( $-0.64$  vs.  $-0.79 \text{ W m}^{-2}$ ). Similarly, differences in  $DRE^{LW}$  and  $DRE^{NET}$  also reduce  
579 significantly. It indicates that the global mean DAOD magnitude difference is more important than  
580 the subtle difference in spatial pattern. Nevertheless, after scaling to the same global mean DAOD  
581 there is still more than 10% difference between the two dust  $DRE^{SW}$ , with CALIOP-based being  
582 the more positive one. This is probably because CALIOP-based DAOD is more concentrated over  
583 dust sources where dust aerosols induce less negative or even positive  $DRE^{SW}$  (For example the  
584 positive  $DRE^{SW}$  over the Sahara Desert and Arabia shown in Figure 10), which result in a less  
585 negative global mean  $DRE^{SW}$  than MODIS.



586



587 Figure 10. Annual mean dust DRE global distribution based on CALIOP-based and MODIS-based DAOD  
588 climatology. MeanSWRI-MeanLWRI-Spheroid dust model are used to represent dust RI and shape in the calculation.  
589 Campaign-PSD is used to represent dust PSD, specifically, Fennec-Fresh PSD is used to represent dust PSD over the  
590 three major dust source regions indicated by three black boxes. AER-D PSD is used to represent dust PSD over other  
591 regions.

592 Table 4. Globally annual mean DAOD,  $DRE^{SW}$ ,  $DRE^{LW}$  and  $DRE^{NET}$  based on CALIOP DAOD and MODIS DAOD  
593 climatology. Note, values in the parentheses are for the two DAOD scaled to the same value of 0.03.

	$\overline{DAOD}$	$\overline{DRE}^{SW}$ [ $Wm^{-2}$ ]	$\overline{DRE}^{LW}$ [ $Wm^{-2}$ ]	$\overline{DRE}^{NET}$ [ $Wm^{-2}$ ]
CALIOP	0.032 (0.03)	-0.69 (-0.64)	0.25 (0.23)	-0.44 (-0.41)
MODIS	0.047 (0.03)	-1.24 (-0.79)	0.34 (0.22)	-0.90 (-0.57)

594

### 595 5.3 Global dust clear-sky DRE based on different dust PSD

596 In the section 5.2, we showed the dust DRE based on the Campaign-PSD. As aforementioned,  
597 one of the main advantages of our size-resolved DREE is that it can be combined with different  
598 dust PSDs to estimate the dust DRE. To demonstrate this, we calculate another set of dust DRE  
599 based on the Kok2017-PSD. Table 5 describes the two dust PSDs used for global dust DRE  
600 calculations and their references. Kok2017-PSD is a globally averaged dust PSD and used to  
601 represent dust PSD for each dusty grid cell. It is constrained with observations and includes coarse  
602 dust particles up to  $20\mu m$ . Although our primary goal here is to demonstrate the capability of our  
603 size-resolved DREE, the comparison between the two DRE can also help us understand the  
604 impacts of dust PSD uncertainty on the dust DRE estimation. Moreover, we also investigate the  
605 sensitivity of DRE to dust RI and dust shape explicitly in this section. The same DAOD  
606 climatology (CALIOP-based DAOD climatology) is used for dust DRE calculations to eliminate  
607 the impact of dust loading difference.

608 Several recent observation-constrained dust PSDs (e.g., Di Biagio et al., 2020, Adebisi et  
609 al., 2020) suggest that dust size is coarser than Kok2017-PSD. As such, Kok2017-PSD is used to  
610 represent the lower limit of the observation-based global dust PSD to investigate the sensitivity of  
611 dust DRE to dust PSD. The Campaign-PSD is purely based on aircraft in-situ measurements and



612 the aircraft was extensively equipped to measure giant particles with diameter larger than  $20\mu\text{m}$ .  
613 We use the dust PSD measured over Sahara (from the Fennec field campaign) to represent dust  
614 PSD over three major dust source regions and use dust PSD measured in the Saharan Air Layer  
615 over the tropical eastern Atlantic (from AER-D field campaign) to represent dust PSD over dust  
616 transport regions. Of course, representing the spatially and temporally variation of global dust PSD  
617 with only two PSDs from the field campaigns is only a crude approximation due to the lack of  
618 PSD measurements. Dust aerosol over the three wide dust source regions may not be all uplifted  
619 within 12 hours as in the Fennec-Fresh measurements, in addition, dust size after long-range  
620 transport could be a bit finer than dust PSD measured over tropical eastern Atlantic (Weinzierl et  
621 al., 2017). Thus, Campaign-PSD likely represents the upper limit of the observation-based global  
622 dust PSD for the investigation of sensitivity to dust PSD. By contrast, the climate models miss  
623 most of coarse dust ( $D > 5\mu\text{m}$ ) in the atmosphere (Adebiyi and Kok, 2020), as a result, the purely  
624 modeled dust PSD without observational constraints will lead to a substantially different dust DRE.  
625 Therefore, the sensitivity test to dust PSD conducted in this study can only represent the  
626 uncertainty induced by the current understanding of observation-based dust PSD.

627 Table 5. The two observation-based dust PSDs used in DRE calculations (see Figure 7).

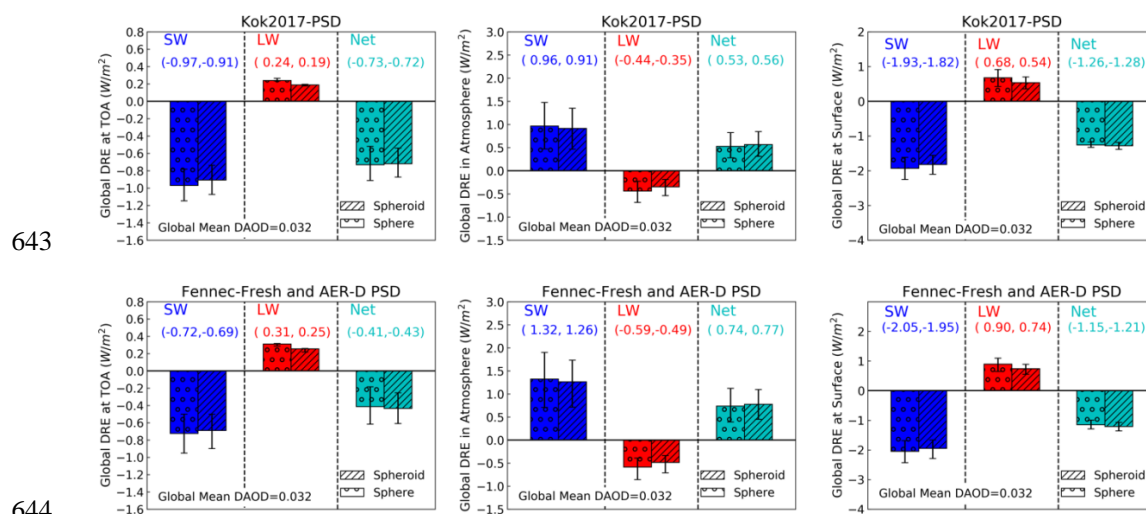
PSD	Description	Reference
Kok2017-PSD	A globally averaged atmospheric PSD derived from observation constrained globally averaged emitted PSD and model simulated globally averaged dust lifetime. This globally averaged PSD is used to represent dust PSD for each dusty grid cell. Dust diameter is cutoff at $20\mu\text{m}$ (Figure 2a in Kok et al.2017).	Kok et al. (2017)
Campaign-PSD	Fennec-Fresh PSD is used for three major dust source regions (i.e., Sahara ( $14\text{-}30^\circ\text{N}$ , $15^\circ\text{W}$ - $30^\circ\text{E}$ ), Middle East ( $10\text{-}35^\circ\text{N}$ , $40\text{-}85^\circ\text{E}$ ) and eastern Asia ( $30\text{-}50^\circ\text{N}$ , $75\text{-}130^\circ\text{E}$ )), which are indicated by the three black boxes in Figure 10. AER-D PSD is used for other regions.	Ryder et al. (2013a, b, 2018, 2019)

628

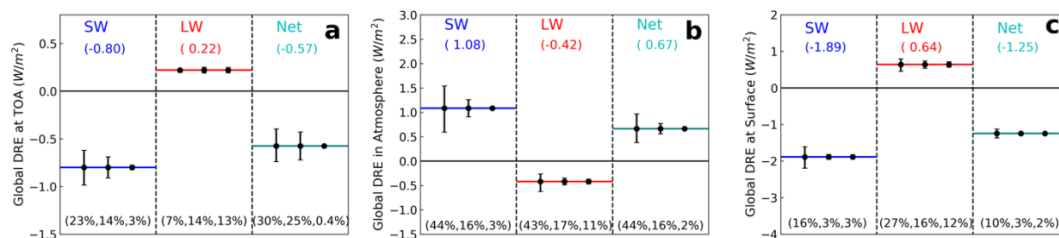
629 We calculated dust DRE of each grid cell ( $DRE_{i,j}$ ) using *DREE-integration* method based  
630 on the dust PSD described in Table 5. Global mean dust DRE was then calculated by averaging



631 dust  $DRE_{i,j}$  weighted by its surface area. Figure 11 shows the global mean  $DRE^{SW}$ ,  $DRE^{LW}$  and  
 632  $DRE^{NET}$  at TOA, surface, and in the atmosphere calculated based on the two sets of PSDs.  
 633 Obviously, Kok2017-PSD leads to stronger cooling effect in SW and weaker warming effect in  
 634 LW at TOA compared to Campaign-PSD, which is consistent with the fact that Kok2017-PSD is  
 635 finer than the Campaign-PSD. In addition, we explicitly include the effects of dust RI and dust  
 636 shape on DRE in Figure 11. Comparison of uncertainty induced by dust PSD, RI and shape  
 637 suggests that dust RI uncertainty leads to the largest uncertainty in dust DRE, particularly RI  
 638 uncertainty induces more than 40% uncertainty in  $DRE^{SW}$  estimations in the atmosphere (Figure  
 639 12). Dust PSD is also important for quantifying dust DRE, we found that the observation-based  
 640 dust PSD uncertainty induces around 15%~20% uncertainty in dust DRE at TOA and in the  
 641 atmosphere. Dust non-sphericity causes a negligible uncertainty in global mean dust DRE, in line  
 642 with previous studies e.g., Raisanen et al. (2013) and Colarco et al. (2014).



645 Figure 11. Globally annual mean clear-sky  $DRE^{SW}$ ,  $DRE^{LW}$  and  $DRE^{NET}$  at TOA, in the atmosphere and surface  
 646 calculated based on the two PSDs described in Table 5. The two rows represent dust DRE based on two PSDs. Error  
 647 bars indicate uncertainty induced by dust RI uncertainty. Different types of bars indicate dust DRE based on different  
 648 dust shapes. This figure explicitly separates the impacts of different dust microphysical properties on dust DRE. Two  
 649 values in parenthesis on each plot represent spherical (left) and spheroidal (right) dust DRE corresponding to mean  
 650 RI.



651

652 Figure 12. Comparison of uncertainty induced by dust RI, PSD and shape in  $DRE^{SW}$ ,  $DRE^{LW}$  and  $DRE^{NET}$  at TOA (a),  
 653 in the atmosphere (b) and surface (c). The horizontal lines in each plot represent global mean  $DRE^{SW}$  (blue line in the  
 654 left column),  $DRE^{LW}$  (red line in the middle column) and  $DRE^{NET}$  (green line in the right column) averaged over two  
 655 dust PSDs (i.e., Kok2017-PSD and Campaign-PSD) based on MeanRI-Spheroid dust model. The three error bars in  
 656 each column represent DRE uncertainty induced by dust RI (left), dust PSD (middle) and dust shape (right).  
 657 Accordingly, the percentage values on the bottom represent the percentage uncertainty induced by dust RI, PSD and  
 658 shape, respectively.

659 It is tempting to compare our global mean dust DRE with results reported in Kok et al. (2017).

660 But it must be noted that the global mean dust DRE shown in Figure 11 is for *clear sky* only, while  
 661 the global mean dust DRE reported in Kok et al. (2017) is for *all sky*. The all-sky dust DRE can  
 662 be separated into contributions from clear-sky and cloudy-sky portions (Myhre et al., 2020):

$$DRE_{all-sky} = (1 - CF) \times DRE_{clear-sky} + CF \times DRE_{cloudy-sky}, \quad (8)$$

663 where  $CF$  is cloud fraction,  $DRE_{clear-sky}$  is dust DRE simulated under the case of removing all  
 664 clouds,  $DRE_{cloudy-sky}$  is the dust DRE assuming whole grid is covered by clouds. To compare  
 665 our global mean dust  $DRE^{SW}$  based on Kok2017-PSD with the results reported in Kok et al. (2017),  
 666 we convert our clear-sky  $DRE_{clear-sky}^{SW}$  to  $DRE_{all-sky}^{SW}$  by using MODIS L3 monthly mean cloud  
 667 fraction. Specifically, we multiply  $DRE_{clear-sky}^{SW}$  by  $(1-CF)$  for each grid cell and then calculate  
 668 global annual mean values. In this process, we neglect the cloudy-sky dust  $DRE^{SW}$  portion because  
 669 the annual mean cloudy-sky dust  $DRE^{SW}$  is estimated to be very small, around  $-0.04$  (Zhang et  
 670 al., 2016). Finally, our estimated global mean  $DRE_{all-sky}^{SW}$  corresponding to  $DAOD=0.03$  is around  
 671  $-0.34 \text{ Wm}^{-2}$ . Although it is comparable to the  $-0.48 \text{ Wm}^{-2}$  from Kok et al. 2017, the following  
 672 differences between the two studies must be kept in mind when interpreting the results. First, the



673 rough conversion from global mean  $DRE_{clear-sky}^{SW}$  to global mean  $DRE_{all-sky}^{SW}$  is subject to the  
674 approximation of global mean  $DRE_{cloudy-sky} \sim 0$  and the MODIS L3 cloud fraction could be  
675 different from modeled cloud fraction used in Kok et al. (2017). Second, the two studies use  
676 different dust RI. Third, in this study Kok2017-PSD is used to represent dust PSD in each dusty  
677 grid and applied to our size-resolved dust DREE dataset to calculate global dust DRE. In contrast,  
678 the model-simulated dust DREE in Kok et al. (2017) has reduced cooling from SW scattering and  
679 enhanced warming from SW absorption effects because the short lifetime of coarse dust in models  
680 concentrates these particles over bright deserts. Fourth, the two studies use different dust shape  
681 models, Kok et al. (2017) accounts for more nonspherical shape model (i.e., tri-axial ellipsoids).  
682 Here we do not compare our global mean  $DRE_{clear-sky}^{LW}$  with  $DRE_{all-sky}^{LW}$  suggested in Kok et al.  
683 (2017) because that the lack of knowledge in  $DRE_{cloudy-sky}^{LW}$  prevent us to convert  $DRE_{clear-sky}^{LW}$   
684 to  $DRE_{all-sky}^{LW}$ . Moreover, the two studies use different dust vertical profile, which is critical for  
685  $DRE^{LW}$  estimations. For instance, dust vertical profile in Kok et al. (2017) is purely based on model  
686 simulations, while this study constrains dust vertical profile with CALIOP observations.  
687 Considering all these factors, it is hard to tell if the comparison is fair.

## 688 **6 Summary and Conclusion**

689 This study developed a clear-sky size-resolved dust DREE dataset in both SW and LW  
690 based on CALIOP-based dust DAOD climatology and dust vertical distributions. The dataset  
691 contains global monthly mean dust DREE at TOA and surface with  $5^\circ$  (longitude)  $\times$   $2^\circ$  (latitude)  
692 spatial resolution for 10 size bins ranging from  $0.1\mu m$  to  $100\mu m$  diameter, for three state-of-the  
693 art dust RI representing more, mean and less absorptive dust, and for two dust shapes representing  
694 spherical and spheroidal dust, respectively.



695           The size-resolved DREE dataset allows us to calculate dust DRE of any DAOD  
696 climatology and dust PSD efficiently by using the *DREE-integration* method presented in section  
697 4.1 without involving radiative transfer simulations. The *DREE-integration* method is proven to  
698 be in great agreement with *conventional* DRE calculations. With the *DREE-integration*  
699 methodology, we firstly calculated clear-sky regional mean  $DREE^{SW}$  and  $DREE^{LW}$  over the Sahara  
700 Desert and tropical Atlantic. The comparison of our calculations with those reported by field  
701 studies based on satellite and ground-based observations shows reasonable agreement. Secondly,  
702 we estimated global mean dust DRE with two satellite-based DAOD climatological datasets and  
703 two different global dust PSDs. We found that the global mean DAOD magnitude difference  
704 between the two DAOD climatological datasets is more important than the subtle difference in  
705 spatial pattern. Nevertheless, after scaling to the same global mean DAOD there is still more than  
706 10% difference between the two dust  $DRE^{SW}$ , with CALIOP-based being the more positive one.  
707 Moreover, our results explicitly show the uncertainty induced by each dust microphysical property  
708 (i.e., dust PSD, RI and shape) separately. When DAOD is constrained: (a) Dust non-sphericity  
709 induces negligible effect on dust DRE estimations; (b) The current understanding of observation-  
710 based dust PSD induces relatively large uncertainty (15%~20%) in dust DRE at TOA and in the  
711 atmosphere (c) Dust RI turns out to be the most important factor in determining dust DRE,  
712 particularly in SW. This implies that better understanding of dust mineral composition and RI will  
713 significantly improve our understanding in dust DRE in the future.

714 *Data availability:*

715           The size-resolved dust DREE dataset and the codes to calculate dust DRE for any given  
716 dust PSD and DAOD are available at  
717 ‘[https://drive.google.com/drive/folders/15\\_e28Y9JiSWiJnIM\\_2flEmt2u6i9phEY?usp=sharing](https://drive.google.com/drive/folders/15_e28Y9JiSWiJnIM_2flEmt2u6i9phEY?usp=sharing)’



718 CALIOP- and MODIS-based DAOD climatological datasets are available at  
719 ‘[https://drive.google.com/drive/folders/1aQVupe7govPwR6qmsqUbr4fJQsp1DBCX?usp=shari](https://drive.google.com/drive/folders/1aQVupe7govPwR6qmsqUbr4fJQsp1DBCX?usp=sharing)  
720 ng’

721

722 *Acknowledgement:*

723 We would like to thank Dr. Claire L. Ryder for providing the Fennec and AER-D dust  
724 PSDs. Qianqian Song and Zhibo Zhang cordially acknowledge the funding support from the Future  
725 Investigators in NASA Earth and Space Science and Technology (FINESST). Zhibo Zhang’s  
726 research is supported by NASA grant (80NSSC20K0130) from the CALIPSO and CloudSat  
727 program. The computations in this study were performed at the UMBC High Performance  
728 Computing Facility (HPCF). The facility is supported by the US National Science Foundation  
729 through the MRI program (grant nos. CNS-0821258 and CNS-1228778) and the SCREMS  
730 program (grant no. DMS-0821311), with substantial support from UMBC.

731



## 732 References

- 733 Adebisi, A. A. and Kok, J. F.: Climate models miss most of the coarse dust in the  
734 atmosphere, *Sci. Adv.*, 6, eaaz9507, <https://doi.org/10.1126/sciadv.aaz9507>, 2020.
- 735 Adebisi, A. A., Kok, J. F., Wang, Y., Ito, A., Ridley, D. A., Nabat, P., and Zhao, C.: Dust  
736 Constraints from joint Observational-Modelling-experimental analysis (DustCOMM):  
737 Comparison with measurements and model simulations, *Atmos. Chem. Phys.*, 20, 829–863,  
738 <https://doi.org/10.5194/acp-20-829-2020>, 2020.
- 739 Albrecht, B. A.: Aerosols, Cloud Microphysics, and Fractional Cloudiness, *Science* (80-. ),  
740 245, 1227–1230, <https://doi.org/10.1126/science.245.4923.1227>, 1989.
- 741 Balkanski, Y., Schulz, M., Claquin, T., and Guibert, S.: Reevaluation of Mineral aerosol  
742 radiative forcings suggests a better agreement with satellite and AERONET data, *Atmos. Chem.*  
743 *Phys.*, 7, 81–95, <https://doi.org/10.5194/acp-7-81-2007>, 2007.
- 744 Di Biagio, C., Formenti, P., Balkanski, Y., Caponi, L., Cazaunau, M., Pangui, E., Journet,  
745 E., Nowak, S., Caquineau, S., Andreae O, M., Kandler, K., Saeed, T., Piketh, S., Seibert, D.,  
746 Williams, E., and Doussin, J. F. C.: Global scale variability of the mineral dust long-wave  
747 refractive index: A new dataset of in situ measurements for climate modeling and remote sensing,  
748 *Atmos. Chem. Phys.*, 17, 1901–1929, <https://doi.org/10.5194/acp-17-1901-2017>, 2017.
- 749 Di Biagio, C., Formenti, P., Balkanski, Y., Caponi, L., Cazaunau, M., Pangui, E., Journet,  
750 E., Nowak, S., Andreae, M. O., Kandler, K., Saeed, T., Piketh, S., Seibert, D., Williams, E., and  
751 Doussin, J. F.: Complex refractive indices and single-scattering albedo of global dust aerosols in  
752 the shortwave spectrum and relationship to size and iron content, *Atmos. Chem. Phys.*, 19, 15503–  
753 15531, <https://doi.org/10.5194/acp-19-15503-2019>, 2019.
- 754 Di Biagio, C., Balkanski, Y., Albani, S., Boucher, O., and Formenti, P.: Direct Radiative  
755 Effect by Mineral Dust Aerosols Constrained by New Microphysical and Spectral Optical Data,  
756 *Geophys. Res. Lett.*, 47, e2019GL086186, <https://doi.org/10.1029/2019GL086186>, 2020.
- 757 Brindley, H. E. and Russell, J. E.: An assessment of Saharan dust loading and the  
758 corresponding cloud-free longwave direct radiative effect from geostationary satellite observations,  
759 *J. Geophys. Res. Atmos.*, 114, <https://doi.org/10.1029/2008JD011635>, 2009.
- 760 Choobari, O. A., P. Zawar-Reza, and Sturman, A.: The global distribution of mineral dust  
761 and its impacts on the climate system: A review, *Atmos. Res.*, 138, 152–165,  
762 <https://doi.org/10.1016/j.atmosres.2013.11.007>, 2014.
- 763 Colarco, P. R., Nowotnick, E. P., Randles, C. A., Yi, B. Q., Yang, P., Kim, K. M., Smith,  
764 J. A., and Bardeen, C. G.: Impact of radiatively interactive dust aerosols in the NASA GEOS-5  
765 climate model: Sensitivity to dust particle shape and refractive index, *J. Geophys. Res.*, 119, 753–  
766 786, <https://doi.org/10.1002/2013jd020046>, 2014.
- 767 Van Der Does, M., Knippertz, P., Zschenderlein, P., Harrison, R. G., and Stuut, J.-B. W.:  
768 The mysterious long-range transport of giant mineral dust particles, *Sci. Adv.*, 4, 1–9, 2018.
- 769 Dubovik, O., Sinyuk, A., Lapyonok, T., Holben, B. N., Mishchenko, M., Yang, P., Eck, T.  
770 F., Volten, H., Munoz, O., Veihelmann, B., van der Zande, W. J., Leon, J. F., Sorokin, M., and  
771 Slutsker, I.: Application of spheroid models to account for aerosol particle nonsphericity in remote  
772 sensing of desert dust, *J. Geophys. Res.*, 111, <https://doi.org/10.1029/2005jd006619>,  
773 2006.
- 774 Dufresne, J. L., Gautier, C., and Ricchiuzzi, P.: Longwave scattering effects of mineral  
775 aerosols, *J. Atmos. Sci.*, 59, 1959–1966, [https://doi.org/10.1175/1520-0469\(2002\)059<1959:LSEOMA>2.0.CO;2](https://doi.org/10.1175/1520-0469(2002)059<1959:LSEOMA>2.0.CO;2), 2002.



- 777           García, O. E., Díez, A. M., Expósito, F. J., Díaz, J. P., Dubovik, O., Dubuisson, P., Roger,  
778 J. C., Eck, T. F., Sinyuk, A., Derimian, Y., Dutton, E. G., Schafer, J. S., Holben, B., and García,  
779 C. A.: Validation of AERONET estimates of atmospheric solar fluxes and aerosol radiative forcing  
780 by ground-based broadband measurements, *J. Geophys. Res. Atmos.*, 113,  
781 <https://doi.org/10.1029/2008JD010211>, 2008.
- 782           Gelaro, R., McCarty, W., Suárez, M. J., Todling, R., Molod, A., Takacs, L., Randles, C.  
783 A., Darmenov, A., Bosilovich, M. G., Reichle, R., Wargan, K., Coy, L., Cullather, R., Draper, C.,  
784 Akella, S., Buchard, V., Conaty, A., da Silva, A. M., Gu, W., Kim, G. K., Koster, R., Lucchesi, R.,  
785 Merkova, D., Nielsen, J. E., Partyka, G., Pawson, S., Putman, W., Rienecker, M., Schubert, S. D.,  
786 Sienkiewicz, M., and Zhao, B.: The modern-era retrospective analysis for research and  
787 applications, version 2 (MERRA-2), *J. Clim.*, 30, 5419–5454, <https://doi.org/10.1175/JCLI-D-16-0758.1>, 2017.
- 789           Ginoux, P., Prospero, J. M., Gill, T. E., Hsu, N. C., and Zhao, M.: Global-scale attribution  
790 of anthropogenic and natural dust sources and their emission rates based on MODIS Deep Blue  
791 aerosol products, <https://doi.org/10.1029/2012RG000388>, 1 September 2012.
- 792           Gkikas, A., Proestakis, E., Amiridis, V., Kazadzis, S., Di Tomaso, E., Tsekeri, A., Marinou,  
793 E., Hatzianastassiou, N., and Pérez García-Pando, C.: ModIs Dust AeroSol (MIDAS): A global  
794 fine-resolution dust optical depth data set, *Atmos. Meas. Tech.*, 14, 309–334,  
795 <https://doi.org/10.5194/amt-14-309-2021>, 2021.
- 796           Hansell, R. A., Tsay, S. C., Ji, Q., Hsu, N. C., Jeong, M. J., Wang, S. H., Reid, J. S., Liou,  
797 K. N., and Ou, S. C.: An assessment of the surface longwave direct radiative effect of airborne  
798 Saharan dust during the NAMMA field campaign, *J. Atmos. Sci.*, 67, 1048–1065,  
799 <https://doi.org/10.1175/2009JAS3257.1>, 2010.
- 800           Hsu, N. C., Jeong, M.-J., Bettenhausen, C., Sayer, A. M., Hansell, R., Seftor, C. S., Huang,  
801 J., and Tsay, S.-C.: Enhanced Deep Blue aerosol retrieval algorithm: The second generation, *J.*  
802 *Geophys. Res. Atmos.*, 118, 9296–9315, <https://doi.org/10.1002/jgrd.50712>, 2013.
- 803           Huang, Y., Kok, J. F., Kandler, K., Lindqvist, H., Nousiainen, T., Sakai, T., Adebisi, A.,  
804 and Jokinen, O.: Climate Models and Remote Sensing Retrievals Neglect Substantial Desert Dust  
805 Asphericity, *Geophys. Res. Lett.*, 47, <https://doi.org/10.1029/2019GL086592>, 2020.
- 806           van de Hulst, H. C.: *Light scattering by small particles*, Wiley, Hoboken, NJ, 1957.
- 807           Huneus, N., Schulz, M., Balkanski, Y., Griesfeller, J., Prospero, J., Kinne, S., Bauer, S.,  
808 Boucher, O., Chin, M., Dentener, F., Diehl, T., Easter, R., Fillmore, D., Ghan, S., Ginoux, P., Grini,  
809 A., Horowitz, L., Koch, D., Krol, M. C., Landing, W., Liu, X., Mahowald, N., Miller, R., Morcrette,  
810 J. J., Myhre, G., Penner, J., Perlwitz, J., Stier, P., Takemura, T., and Zender, C. S.: Global dust  
811 model intercomparison in AeroCom phase i, *Atmos. Chem. Phys.*, 11, 7781–7816,  
812 <https://doi.org/10.5194/acp-11-7781-2011>, 2011.
- 813           Kato, S., Rose, F. G., Sun-Mack, S., Miller, W. F., Chen, Y., Rutan, D. A., Stephens, G.  
814 L., Loeb, N. G., Minnis, P., Wielicki, B. A., Winker, D. M., Charlock, T. P., Stackhouse, P. W.,  
815 Xu, K. M., and Collins, W. D.: Improvements of top-of-atmosphere and surface irradiance  
816 computations with CALIPSO-, CloudSat-, and MODIS-derived cloud and aerosol properties, *J.*  
817 *Geophys. Res.*, 116, <https://doi.org/10.1029/2011jd016050>, 2011.
- 818           Kaufman, Y. J., Koren, I., Remer, L. A., Tanré, D., Ginoux, P., and Fan, S.: Dust transport  
819 and deposition observed from the Terra-Moderate Resolution Imaging Spectroradiometer  
820 (MODIS) spacecraft over the Atlantic Ocean, *J. Geophys. Res. D Atmos.*, 110, 1–16,  
821 <https://doi.org/10.1029/2003JD004436>, 2005.
- 822           Koffi, B., Schulz, M., Bréon, F. M., Griesfeller, J., Winker, D., Balkanski, Y., Bauer, S.,



- 823 Berntsen, T., Chin, M., Collins, W. D., Dentener, F., Diehl, T., Easter, R., Ghan, S., Ginoux, P.,  
824 Gong, S., Horowitz, L. W., Iversen, T., Kirkevg, A., Koch, D., Krol, M., Myhre, G., Stier, P., and  
825 Takemura, T.: Application of the CALIOP layer product to evaluate the vertical distribution of  
826 aerosols estimated by global models: AeroCom phase i results,  
827 <https://doi.org/10.1029/2011JD016858>, 2012.
- 828 Li, F., Vogelmann, A. M., and Ramanathan, V.: Saharan dust aerosol radiative forcing  
829 measured from space, *J. Clim.*, 17, 2558–2571, [https://doi.org/Doi 10.1175/1520-0442\(2004\)017<2558:Sdarfm>2.0.Co;2](https://doi.org/Doi%2010.1175/1520-0442(2004)017<2558:Sdarfm>2.0.Co;2), 2004.
- 831 Mahowald, N., Albani, S., Kok, J. F., Engelstaeder, S., Scanza, R., Ward, D. S., and Flanner,  
832 M. G.: The size distribution of desert dust aerosols and its impact on the Earth system,  
833 <https://doi.org/10.1016/j.aeolia.2013.09.002>, 1 December 2014.
- 834 Meloni, D., di Sarra, A., Di Iorio, T., and Fiocco, G.: Influence of the vertical profile of  
835 Saharan dust on the visible direct radiative forcing, *J. Quant. Spectrosc. Radiat. Transf.*, 93, 397–  
836 413, <https://doi.org/10.1016/j.jqsrt.2004.08.035>, 2005.
- 837 Meloni, D., Junkermann, W., di Sarra, A., Cacciani, M., De Silvestri, L., Di Iorio, T.,  
838 Estellés, V., Gómez-Amo, J. L., Pace, G., and Sferlazzo, D. M.: Altitude-resolved shortwave and  
839 longwave radiative effects of desert dust in the Mediterranean during the GAMARF campaign:  
840 Indications of a net daily cooling in the dust layer, *J. Geophys. Res.*, 120, 3386–3407,  
841 <https://doi.org/10.1002/2014JD022312>, 2015.
- 842 Meng, Z. K., Yang, P., Kattawar, G. W., Bi, L., Liou, K. N., and Laszlo, I.: Single-  
843 scattering properties of tri-axial ellipsoidal mineral dust aerosols: A database for application to  
844 radiative transfer calculations, *J. Aerosol Sci.*, 41, 501–512,  
845 <https://doi.org/10.1016/j.jaerosci.2010.02.008>, 2010.
- 846 Mlawer, E. J. and Clough, S. A.: Shortwave and longwave enhancements in the rapid  
847 radiative transfer model, *Proc. Seventh Atmos. Radiat. Meas. Sci. Team Meet.*, 409–413, 1998.
- 848 Mlawer, E. J., Taubman, S. J., Brown, P. D., Iacono, M. J., and Clough, S. A.: Radiative  
849 transfer for inhomogeneous atmospheres: RRTM, a validated correlated-k model for the longwave,  
850 *J. Geophys. Res. Atmos.*, 102, 16663–16682, <https://doi.org/10.1029/97jd00237>, 1997.
- 851 Myhre, G., Grini, A., Haywood, J. M., Stordal, F., Chatenet, B., Tanre, D., Sundet, J. K.,  
852 and Isaksen, I. S. A.: Modeling the radiative impact of mineral dust during the Saharan Dust  
853 Experiment (SHADE) campaign, *J. Geophys. Res.*, 108, [https://doi.org/Artn 8579](https://doi.org/Artn%208579)  
854 [10.1029/2002jd002566](https://doi.org/10.1029/2002jd002566), 2003.
- 855 Myhre, G., Samset, B. H., Mohr, C. W., Alterskjær, K., Balkanski, Y., Bellouin, N., Chin,  
856 M., Haywood, J., Hodnebrog, O., Kinne, S., Lin, G., Lund, M. T., Penner, J. E., Schulz, M.,  
857 Schutgens, N., Skeie, R. B., Stier, P., Takemura, T., and Zhang, K.: Cloudy-sky contributions to  
858 the direct aerosol effect, *Atmos. Chem. Phys.*, 20, 8855–8865, <https://doi.org/10.5194/acp-20-8855-2020>, 2020.
- 860 Patadia, F., Yang, E. S., and Christopher, S. A.: Does dust change the clear sky top of  
861 atmosphere shortwave flux over high surface reflectance regions?, *Geophys. Res. Lett.*, 36,  
862 <https://doi.org/10.1029/2009GL039092>, 2009.
- 863 Pu, B. and Ginoux, P.: How reliable are CMIP5 models in simulating dust optical depth?,  
864 *Atmos. Chem. Phys.*, 18, 12491–12510, <https://doi.org/10.5194/acp-18-12491-2018>, 2018.
- 865 Raisanen, P., Haapanala, P., Chung, C. E., Kahnert, M., Makkonen, R., Tonttila, J., and  
866 Nousiainen, T.: Impact of dust particle non-sphericity on climate simulations, *Q. J. R. Meteorol.*  
867 *Soc.*, 139, 2222–2232, <https://doi.org/10.1002/qj.2084>, 2013.
- 868 Remer, L. A., Kaufman, Y. J., Tanré, D., Mattoo, S., Chu, D. A., Martins, J. V., Li, R. R.,



- 869 Ichoku, C., Levy, R. C., Kleidman, R. G., Eck, T. F., Vermote, E., and Holben, B. N.: The MODIS  
870 aerosol algorithm, products, and validation, *J. Atmos. Sci.*, 62, 947–973,  
871 <https://doi.org/10.1175/JAS3385.1>, 2005.
- 872 Ryder, C. L., Highwood, E. J., Lai, T. M., Sodemann, H., and Marsham, J. H.: Impact of  
873 atmospheric transport on the evolution of microphysical and optical properties of Saharan dust,  
874 *Geophys. Res. Lett.*, 40, 2433–2438, <https://doi.org/10.1002/grl.50482>, 2013a.
- 875 Ryder, C. L., Highwood, E. J., Rosenberg, P. D., Trembath, J., Brooke, J. K., Bart, M.,  
876 Dean, A., Crosier, J., Dorsey, J., Brindley, H., Banks, J., Marsham, J. H., McQuaid, J. B.,  
877 Sodemann, H., and Washington, R.: Optical properties of Saharan dust aerosol and contribution  
878 from the coarse mode as measured during the Fenec 2011 aircraft campaign, *Atmos. Chem. Phys.*,  
879 13, 303–325, <https://doi.org/10.5194/acp-13-303-2013>, 2013b.
- 880 Ryder, C. L., Marengo, F., Brooke, J. K., Estelles, V., Cotton, R., Formenti, P., McQuaid,  
881 J. B., Price, H. C., Liu, D., Ausset, P., Rosenberg, P. D., Taylor, J. W., Choularton, T., Bower, K.,  
882 Coe, H., Gallagher, M., Crosier, J., Lloyd, G., Highwood, E. J., and Murray, B. J.: Coarse-mode  
883 mineral dust size distributions, composition and optical properties from AER-D aircraft  
884 measurements over the tropical eastern Atlantic, *Atmos. Chem. Phys.*, 18, 17225–17257,  
885 <https://doi.org/10.5194/acp-18-17225-2018>, 2018.
- 886 Ryder, C. L., Highwood, E. J., Walser, A., Seibert, P., Philipp, A., and Weinzierl, B.:  
887 Coarse and Giant Particles are Ubiquitous in Saharan Dust Export Regions and are Radiatively  
888 Significant over the Sahara, *Atmos. Chem. Phys. Discuss.*, <https://doi.org/10.5194/acp-2019-421>,  
889 2019.
- 890 Sakai, T., Nagai, T., Zaizen, Y., and Mano, Y.: Backscattering linear depolarization ratio  
891 measurements of mineral, sea-salt, and ammonium sulfate particles simulated in a laboratory  
892 chamber, *Appl. Opt.*, 49, 4441–4449, 2010.
- 893 Satheesh, S. K. and Ramanathan, V.: Large differences in tropical aerosol forcing at the  
894 top of the atmosphere and Earth’s surface, *Nature*, 405, 60–63, <https://doi.org/10.1038/35011039>,  
895 2000.
- 896 Sokolik, I. N., Toon, O. B., and Bergstrom, R. W.: Modeling the radiative characteristics  
897 of airborne mineral aerosols at infrared wavelengths, *J. Geophys. Res.*, 103, 8813–8826,  
898 <https://doi.org/10.1029/98jd00049>, 1998.
- 899 Song, Q., Zhang, Z., Yu, H., Kato, S., Yang, P., Colarco, P., Remer, L. A., and Ryder, C.  
900 L.: Net radiative effects of dust in the tropical North Atlantic based on integrated satellite  
901 observations and in situ measurements, *Atmos. Chem. Phys.*, 18, [https://doi.org/10.5194/acp-18-  
902 11303-2018](https://doi.org/10.5194/acp-18-11303-2018), 2018.
- 903 Song, Q., Zhang, Z., Yu, H., Ginoux, P., and Shen, J.: Global dust optical depth climatology  
904 derived from CALIOP and MODIS aerosol retrievals on decadal timescales: regional and  
905 interannual variability, *Atmos. Chem. Phys.*, 21, 13369–13395, [https://doi.org/10.5194/acp-21-  
906 13369-2021](https://doi.org/10.5194/acp-21-13369-2021), 2021.
- 907 Stamnes, K., Tsay, S.-C., Wiscombe, W., and Jayaweera, K.: Numerically stable algorithm  
908 for discrete-ordinate-method radiative transfer in multiple scattering and emitting layered media,  
909 *Appl. Opt.*, 27, 2502, <https://doi.org/10.1364/ao.27.002502>, 1988.
- 910 Tegen, I. and Lacis, A. A.: Modeling of particle size distribution and its influence on the  
911 radiative properties of mineral dust aerosol, *J. Geophys. Res. Atmos.*, 101, 19237–19244,  
912 <https://doi.org/10.1029/95jd03610>, 1996.
- 913 Tegen, I., Lacis, A. A., and Fung, I.: The influence on climate forcing of mineral aerosols  
914 from disturbed soils, *Nature*, 380, 419–422, <https://doi.org/10.1038/380419a0>, 1996.



- 915 Textor, C., Schulz, M., Guibert, S., Kinne, S., Balkanski, Y., Bauer, S., Bernsten, T.,  
916 Berglen, T., Boucher, O., Chin, M., Dentener, F., Diehl, T., Easter, R., Feichter, H., Fillmore, D.,  
917 Ghan, S., Ginoux, P., Gong, S., Kristjansson, J. E., Krol, M., Lauer, A., Lamarque, J. F., Liu, X.,  
918 Montanaro, V., Myhre, G., Penner, J., Pitari, G., Reddy, S., Seland, O., Stier, P., Takemura, T.,  
919 and Tie, X.: Analysis and quantification of the diversities of aerosol life cycles within AeroCom,  
920 *Atmos. Chem. Phys.*, 6, 1777–1813, 2006.
- 921 Twomey, S.: The influence of pollution on the shortwave albedo of clouds, *J. Atmos. Sci.*,  
922 34, 1149–1152, 1977.
- 923 Voss, K. K. and Evan, A. T.: A New Satellite-Based Global Climatology of Dust Aerosol  
924 Optical Depth, *J. Appl. Meteorol. Climatol.*, 59, 83–102, [https://doi.org/10.1175/JAMC-D-19-](https://doi.org/10.1175/JAMC-D-19-2020)  
925 2020.
- 926 Vouk, V.: Projected area of convex bodies [3], <https://doi.org/10.1038/162330a0>, 1948.
- 927 Weinzierl, B., Ansmann, A., Prospero, J. M., Althausen, D., Benker, N., Chouza, F.,  
928 Dollner, M., Farrell, D., Fomba, W. K., Freudenthaler, V., Gasteiger, J., Gross, S., Haerig, M.,  
929 Heinold, B., Kandler, K., Kristensen, T. B., Mayol-Bracero, O. L., Müller, T., Reitebuch, O., Sauer,  
930 D., Schafner, A., Schepanski, K., Spanu, A., Tegen, I., Toledano, C., and Walser, A.: THE  
931 SAHARAN AEROSOL LONG-RANGE TRANSPORT AND AEROSOL-CLOUD-  
932 INTERACTION EXPERIMENT Overview and Selected Highlights, *Bull. Am. Meteorol. Soc.*,  
933 98, 1427–1451, <https://doi.org/10.1175/Bams-D-15-00142.1>, 2017.
- 934 Winker, D. M., Vaughan, M. A., Omar, A., Hu, Y., Powell, K. A., Liu, Z., Hunt, W. H.,  
935 and Young, S. A.: Overview of the CALIPSO mission and CALIOP data processing algorithms,  
936 *J. Atmos. Ocean. Technol.*, 26, 2310–2323, <https://doi.org/10.1175/2009JTECHA1281.1>, 2009.
- 937 Wiscombe, W. J.: Improved Mie Scattering Algorithms, *Appl. Opt.*, 19, 1505–1509,  
938 <https://doi.org/Doi.10.1364/Ao.19.001505>, 1980.
- 939 Wu, M., Liu, X., Yu, H., Wang, H., Shi, Y., Yang, K., Darmenov, A., Wu, C., Wang, Z.,  
940 Luo, T., Feng, Y., and Ke, Z.: Understanding processes that control dust spatial distributions with  
941 global climate models and satellite observations, *Atmos. Chem. Phys.*, 20, 13835–13855,  
942 <https://doi.org/10.5194/acp-20-13835-2020>, 2020.
- 943 Yu, H., Kaufman, Y. J., Chin, M., Feingold, G., Remer, L. A., Anderson, T. L., Balkanski,  
944 Y., Bellouin, N., Boucher, O., Christopher, S., DeCola, P., Kahn, R., Koch, D., Loeb, N., Reddy,  
945 M. S., Schulz, M., Takemura, T., and Zhou, M.: A review of measurement-based assessments of  
946 the aerosol direct radiative effect and forcing, *Atmos. Chem. Phys.*, 6, 613–666, 2006.
- 947 Yu, H., Chin, M., Remer, L. A., Kleidman, R. G., Bellouin, N., Bian, H., and Diehl, T.:  
948 Variability of marine aerosol fine-mode fraction and estimates of anthropogenic aerosol  
949 component over cloud-free oceans from the Moderate Resolution Imaging Spectroradiometer  
950 (MODIS), *J. Geophys. Res. Atmos.*, 114, <https://doi.org/10.1029/2008JD010648>, 2009.
- 951 Yu, H., Chin, M., Winker, D. M., Omar, A. H., Liu, Z., Kittaka, C., and Diehl, T.: Global  
952 view of aerosol vertical distributions from CALIPSO lidar measurements and GOCART  
953 simulations: Regional and seasonal variations, *J. Geophys. Res. Atmos.*, 115, 1–19,  
954 <https://doi.org/10.1029/2009JD013364>, 2010.
- 955 Yu, H., Tan, Q., Chin, M., Remer, L. A., Kahn, R. A., Bian, H., Kim, D., Zhang, Z., Yuan,  
956 T., Omar, A. H., Winker, D. M., Levy, R. C., Kalashnikova, O., Crepeau, L., Capelle, V., and  
957 Chédin, A.: Estimates of African Dust Deposition Along the Trans-Atlantic Transit Using the  
958 Decadelong Record of Aerosol Measurements from CALIOP, MODIS, MISR, and IASI, *J.*  
959 *Geophys. Res. Atmos.*, 124, 7975–7996, <https://doi.org/10.1029/2019JD030574>, 2019.
- 960 Yu, H., Yang, Y., Wang, H., Tan, Q., Chin, M., Levy, R., Remer, L., Smith, S., Yuan, T.,



- 961 and Shi, Y.: Interannual Variability and Trends of Combustion Aerosol and Dust in Major  
962 Continental Outflows Revealed by MODIS Retrievals and CAM5 Simulations During 2003–2017,  
963 *Atmos. Chem. Phys. Discuss.*, 1–38, <https://doi.org/10.5194/acp-2019-621>, 2020.
- 964 Zhang, J. L. and Christopher, S. A.: Longwave radiative forcing of Saharan dust aerosols  
965 estimated from MODIS, MISR, and CERES observations on Terra, *Geophys. Res. Lett.*, 30,  
966 <https://doi.org/Artn 2188 10.1029/2003gl018479>, 2003.
- 967 Zhang, Z. B., Meyer, K., Yu, H. B., Platnick, S., Colarco, P., Liu, Z. Y., and Oreopoulos,  
968 L.: Shortwave direct radiative effects of above-cloud aerosols over global oceans derived from 8  
969 years of CALIOP and MODIS observations, *Atmos. Chem. Phys.*, 16, 2877–2900,  
970 <https://doi.org/10.5194/acp-16-2877-2016>, 2016.
- 971 Zheng, J., Zhang, Z., Garnier, A., Yu, H., Song, Q., Wang, C., Dubuisson, P., and Di Biagio,  
972 C.: The thermal infrared optical depth of mineral dust retrieved from integrated CALIOP and IIR  
973 observations, *Remote Sens. Environ.*, 270, <https://doi.org/10.1016/j.rse.2021.112841>, 2022.
- 974 Zhou, M., Yu, H., Dickinson, R. E., Dubovik, O., and Holben, B. N.: A normalized  
975 description of the direct effect of key aerosol types on solar radiation as estimated from Aerosol  
976 Robotic Network aerosols and Moderate Resolution Imaging Spectroradiometer albedos, *J.*  
977 *Geophys. Res. D Atmos.*, 110, 1–10, <https://doi.org/10.1029/2005JD005909>, 2005.  
978